Supporting Information for the paper

Theoretical Study of Sensitive Reactions in Phenol Decomposition

Luna Pratali Maffei, Matteo Pelucchi, Tiziano Faravelli and Carlo Cavallotti*

CRECK Modeling Lab, Department of Chemistry, Materials, and Chemical Engineering. Politecnico di Milano, Italy.

TABLE OF CONTENTS

Attached files:

a. Rate constants of the single channels of phenol decomposition (file: rate_constants_PES_C6H5OH.txt)
b. Rate constants of the single channels of phenoxy decomposition (file: rate_constants_PES_C6H5O.txt)
c. Mess input file for phenol decomposition (file: mess_C6H5OH.txt)
d. Mess input file for phenoxy decomposition (file: mess_C6H5O.txt)
e. Mess input files for H-atom abstraction on phenol, on the different sites (files: mess_C6H5OH_HABS_OH.txt, mess_C6H5OH_HABS_ring_orto.txt, mess_C6H5OH_HABS_ring_meta.txt, mess_C6H5OH_HABS_ring_para.txt)
f. Mess input files for H-atom abstraction on cyclopentadiene (file: mess_C5H6_HABS.txt)
g. Kinetic model (CKI, CKT and transport properties files)

1. Multireference diagnostics for the decarbonylation channel

As anticipated in the main text, we investigated the multi-reference (MR) character of the rate determining step of the molecular decomposition of phenol, namely the decarbonylation channel. MR methods are often needed to describe accurately bond dissociation processes that involve electronic states which are close in energy. Due to both the relevant difference between the energy barrier computed for the decarbonylation step and the previous literature studies,[1,2] and the peculiar geometry of the TS of this reaction pathway, we carefully investigated the MR character of this elementary step in order to choose an appropriate theoretical treatment. In particular, we followed some of the procedures recently listed by Jalan et al.,[3] that cover an extensive set of MR diagnostics methods.

The decarbonylation T1 diagnostic, the most common way to identify MR character,[4] computed at the CCSD(T)/aug-cc-pVTZ level is 0.016, thus below the recommended threshold of 0.02. As explained in the main text, additional calculations were performed to determine the multireference character of the reaction. The results of these calculations are summarized in Table S1. The B1 diagnostics[5] is based on the energy difference (in this case the energy barriers of the TS) obtained with two different DFT methods, namely B1LYP and BLYP. B1 is computed as (E_BLYP//BLYP-E_BLYP)/n, where n is the number of broken bonds (in our case, 2). We used two different basis sets, 6-311+G(d,p) and 6-311+G(2df,2p), obtaining close values of about 2.7 kcal/mol. This is below the recommended threshold of 10 kcal/mol, and therefore does not suggest any MR character for this channel. We then analyzed the sensitivity of the coupled cluster energy to the choice of orbitals of the reference function (either Hartree Fock or DFT), called reference orbital diagnostics (ROD).[6] We were unable to apply this method because RCCSD(T) did not converge with any of the DFT functionals used (BLYP, B3LYP, ωB97X-D). This was a first evidence of the peculiarity of the characteristics of the orbitals of this TS. The diagnostics indicating that the reaction channel studies possesses a MR character were those based on the total atomization energies (TAE), proposed by Karton and coworkers.[7] In particular, the %TAE(SCF) compares the TAE obtained at the highest level of theory used (CCSD(T)/aug-cc-pVTZ in this case) with the TAE obtained by a single-reference SCF calculation. %TAE(SCF) was thus computed as (TAE(CCSD(T))-TAE(HF))/TAE(CCSD(T))*100%, using aug-cc-pVTZ basis set in both cases, on the geometries optimized at ωB97X-D/6-311+G(d,p) level. We obtained a %TAE(SCF) of 28 %, which indicates a fairly large amount of non-dynamical correlation. The %TAE[(T)] diagnostics instead accounts for the contribution of the perturbative triples (T) to the RCCSD(T) energy compared to the RCCSD one, and is defined as (TAE(RCCSD(T))-TAE(RCCSD))/TAE(RCCSD(T))*100%. In this case, the 2.4 % value computed for the present system is slightly higher than the recommended threshold of 2 %, and therefore indicates a mild MR character. Finally, we computed the diagnostics with methods that require the use of MR theories such as CASSCF.[8] In particular, the M diagnostics is defined as (2-n(MCDONO)+n(MCUNO))/2, where n(MCDONO) is the lowest occupation of all doubly occupied natural orbitals, whereas n(MCUNO) is the highest occupation of the unoccupied natural orbitals. Using an active space of (2e,2o), we obtained an M value of 0.08, clearly above the recommended threshold of 0.04. This increases to 0.11 when using an AS of (6e,6o). Finally, the C_0^2 diagnostics, where C_0 is the coefficient of the HF determinant in the multiconfiguration expansion, resulted in a 0.96 value, which is higher than the recommended threshold of 0.9. Further diagnostics based on the variation of the barrier heights using UCCSD(T) or RCCSD(T) instead did not show any significant MR character. Due to the positive results of some of the MR diagnostic methods, we then treated this channel at CASPT2 level of theory, as described below.

Table S1: Multireference diagnostics and recommended values for the decarbonylation channel.

Diagnostic	Value	Recommendation	MR?
B1	2.7 kcal/mol	< 10 kcal/mol	NO
%TAE(SCF)	28%	> 66.7 %	YES
%TAE[(T)]	2.40%	< 2 %	YES,MILD
M	0.08	< 0.04	YES
C_0^2	0.96	> 0.9	NO

In Table S2 and

Table S3, we report the energy barriers determined for the decarbonylation reaction using different levels of theory. The AS used is described in the main text in the method section. Table S2 lists the electronic energies and the ZPE for the TS and the reactant determined on the DFT geometry. Other calculations with an AS of (10e,9o) are not reported here, because we were not able to converge the proper AS for the reactant. In

Table S3, the little difference (< 0.4 kcal/mol) in energy between the (6e,6o) AS and the (12e,11o) AS shows that the AS size has converged. For the final energy (in bold in

Table S3), we applied an IPEA shift of 0.25. The small difference (0.17 kcal/mol) between the CCSD(T)/CBS barriers computed with DFT and CASPT2 geometries also shows that the quality of the geometry is not the main reason for the change between CASPT2 and CCSD(T) energy barriers. Finally, Table S4 shows the effect of the size of the basis set on the final energy barrier. The results show that the energies computed using aug-cc-pVDZ and cc-pVTZ basis sets are up to 2.8 kcal/mol higher than those computed using the aug-cc-pVTZ basis set, though still smaller than those determined at the CCSD(T) level.

Table S2: Energies (Hartrees) and energy barriers (kcal/mol) of the decarbonylation channel determined with the **DFT geometry** optimized at ωB97X-D/aug-cc-pVTZ level.

	ZPE ωB97X-D/ aug-cc-pVTZ	HL CCSD(T)	RS2C(6e,6o)/ aug-cc-pVTZ	RS2C(12e,11o)/ aug-cc-pVTZ	RS2C(12e,11o)/ aug-cc-pVTZ shift = 0.2	RS2C(12e,11o)/ aug-cc-pVTZ IPEA = 0.25
E TS	0.100	-306.914	-306.744	-306.747	-306.742	-306.742
E Reactant	0.103	-306.962	-306.787	-306.786	-306.782	-306.783
EBarrTS (0K)	-1.73	29.91	27.15	24.81	25.05	25.74
EBarrTS(0K)+ZPE		28.18	25.42	23.08	23.32	24.01

Table S3: Energies (Hartree) and energy barriers(kcal/mol) of the decarbonylation reaction determined with the CASPT2(6e,6o)/aug-cc-pVTZ geometry.

	ZPE RS2(6e,6o)/ aug-cc-pVTZ	HL CCSD(T)	RS2(6e,6o)/ aug-cc-pVTZ	RS2C(12e,11o)/ aug-cc-pVTZ	RS2C(12e,11o)/ aug-cc-pVTZ shift = 0.2	RS2C(12e,11o)/ aug-cc-pVTZ IPEA = 0.25
E TS	0.100	-306.914	-306.748	-306.746	-306.742	-306.742
E Reactant	0.103	-306.962	-306.789	-306.787	-306.783	-306.784
EBarr TS(0K)	-1.68	30.03	25.91	25.52	25.74	26.25
EBarrTS(0K)+ZPE		28.35	24.22	23.84	24.06	**24.57**

Table S4: Energies (Hartree) and energy barriers (kcal/mol) of the decarbonylation reaction determined with the CASPT2(6e,6o)/aug-cc-pVTZ geometry.

	ZPE RS2(6e,6o)/ aug-cc-pVTZ	RS2C(12e,11o)/ aug-cc-pVDZ shift = 0.2	RS2C(12e,11o)/ aug-cc-pVDZ IPEA = 0.25	RS2C(12e,11o)/ cc-pVTZ shift = 0.2	RS2C(12e,11o)/ cc-pVTZ IPEA = 0.25
E TS	0.100	-306.476	-306.475	-306.716	-306.716
E Reactant	0.103	-306.519	-306.520	-306.761	-306.762
EBarr TS(0K)	-1.68	27.14	27.96	28.21	29.05
EBarr TS(0K)+ZPE		25.45	26.28	26.53	27.36

2. CCSD(T)-F12 energies for phenol molecular decomposition to C_5H_6+CO

In order to estimate the dependence of the values of the energies on the chosen theoretical method, we computed the energies of the stationary points of the elementary steps of the molecular decomposition of phenol (highlighted in red in Figure 3 of the main text) also at the CCSD(T)-F12/cc-pVTZ level. Calculations at the CCSD(T)-F12/cc-pVQZ level were not performed, since they were too computationally demanding for the investigated system. The extrapolation to the complete basis set limit was performed by adding MP2 corrections (MP2-F12/cc-pVQZ-F12 − MP2-F12/cc-pVTZ-F12). Also, corrections for inclusion of core electrons in CC excitations were computed as CCSD(T)(core)/cc-pcVTZ − CCSD(T)/cc-pVTZ. The values obtained and the extent of the corrections considered are reported in Table S5. The nomenclature of the stationary points refers to Figure 3. The CCSD(T)/CBS values (computed as reported in the Methods section) are about 0.5 kcal/mol lower than those calculated at CCSD(T)-F12/cc-pVTZ level. The largest difference is due to the inclusion of core corrections. An exception to this trend is the decarbonylation channel, whose TS shows almost 1 kcal/mol discrepancy between the two methods. This highlights the peculiar characteristics of this reaction channel.

Table S5: Energies at CCSD(T)-F12/cc-pVTZ level and extent of MP2 and core corrections for the stationary points of the main elementary steps of phenol decomposition to C_5H_6 + CO. The names of the stationary points refer to Figure 3. The comparison between the final values and those obtained at CCSD(T)/CBS level (as described in the main text) is highlighted in bold.

	W1	TS1	W2	TS2	W3	TS3	W4	TS4	C_5H_6	CO
CCSD(T)-F12 [Hartree]	-307.058	-306.942	-307.028	-306.955	-306.962	-306.956	-306.975	-306.927	-193.810	-113.200
[CCSD(T)/cc-pcVTZ - CCSD(T)/cc-pVTZ] [Hartree]	-0.364	-0.364	-0.364	-0.364	-0.363	-0.364	-0.364	-0.363	-0.255	-0.109
[MP2/cc-pVQZ-MP2/cc-pVTZ] [Hartree]	-0.006	-0.005	-0.005	-0.006	-0.006	-0.005	-0.005	-0.005	-0.003	-0.002
CCSD(T)-F12 [kcal/mol]	0.00	68.79	17.97	61.51	57.27	61.81	50.74	79.18	25.87	
+ΔMP2 [kcal/mol]	0.00	68.86	18.04	61.56	57.32	61.88	50.85	79.27	25.91	
+ΔMP2+Δcore [kcal/mol]	**0.00**	**69.03**	**18.24**	**61.85**	**57.69**	**62.24**	**51.05**	**79.74**	**26.12**	
CCSD(T)/CBS [kcal/mol]	**0.00**	**68.70**	**17.80**	**61.40**	**57.10**	**61.60**	**50.50**	**78.70**	**25.80**	

3. Model Validation

a. Phenol pyrolysis (additional targets)
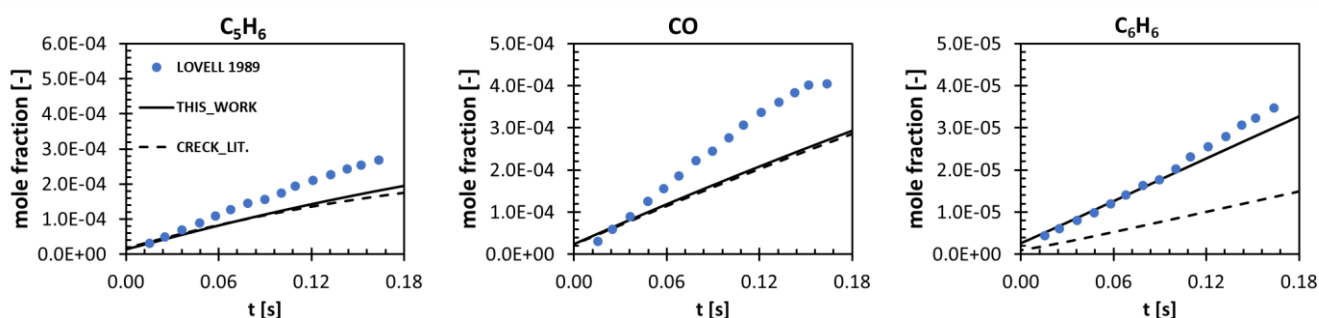
Figure S1: Species profiles of the PFR reactor experiments of Lovell et al. (1168 K, 1 atm)[9]
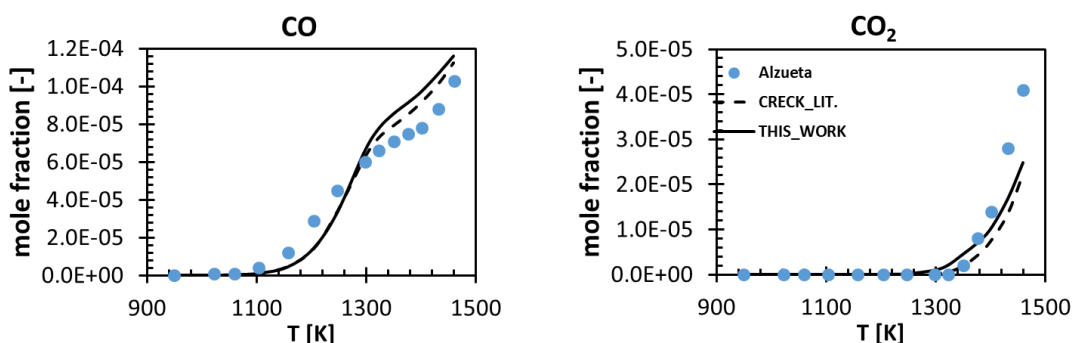
Figure S2a: Species profiles of the PFR experiments for phenol pyrolysis of Alzueta et al.[10]
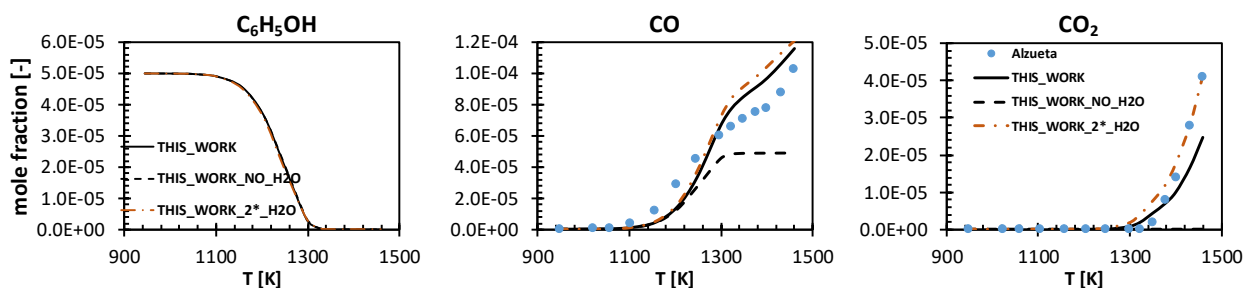
Figure S2b: Species profiles of the PFR experiments for phenol pyrolysis of Alzueta et al.[10] performed with the model developed in this work at varying H_2O inlet concentrations (no H_2O; experimental H_2O concentration; and H_2O concentration doubled with respect to the experimental value). The simulations show that the effect of water co-injection is well described by the adopted phenol decomposition model, which was developed assuming that reactions take place in an Ar bath gas, thus not accounting for H_2O enhanced collisional efficiency. It should however be observed that pressure dependence effects in the present system are significant mostly for the $H+C_6H_5O$ channel. In the case investigated, such reaction plays a major role in the reactivity only above 1400 K, thus in a condition in which phenol is already mostly decomposed.

b) Benzene pyrolysis and oxidation

Pyrolysis
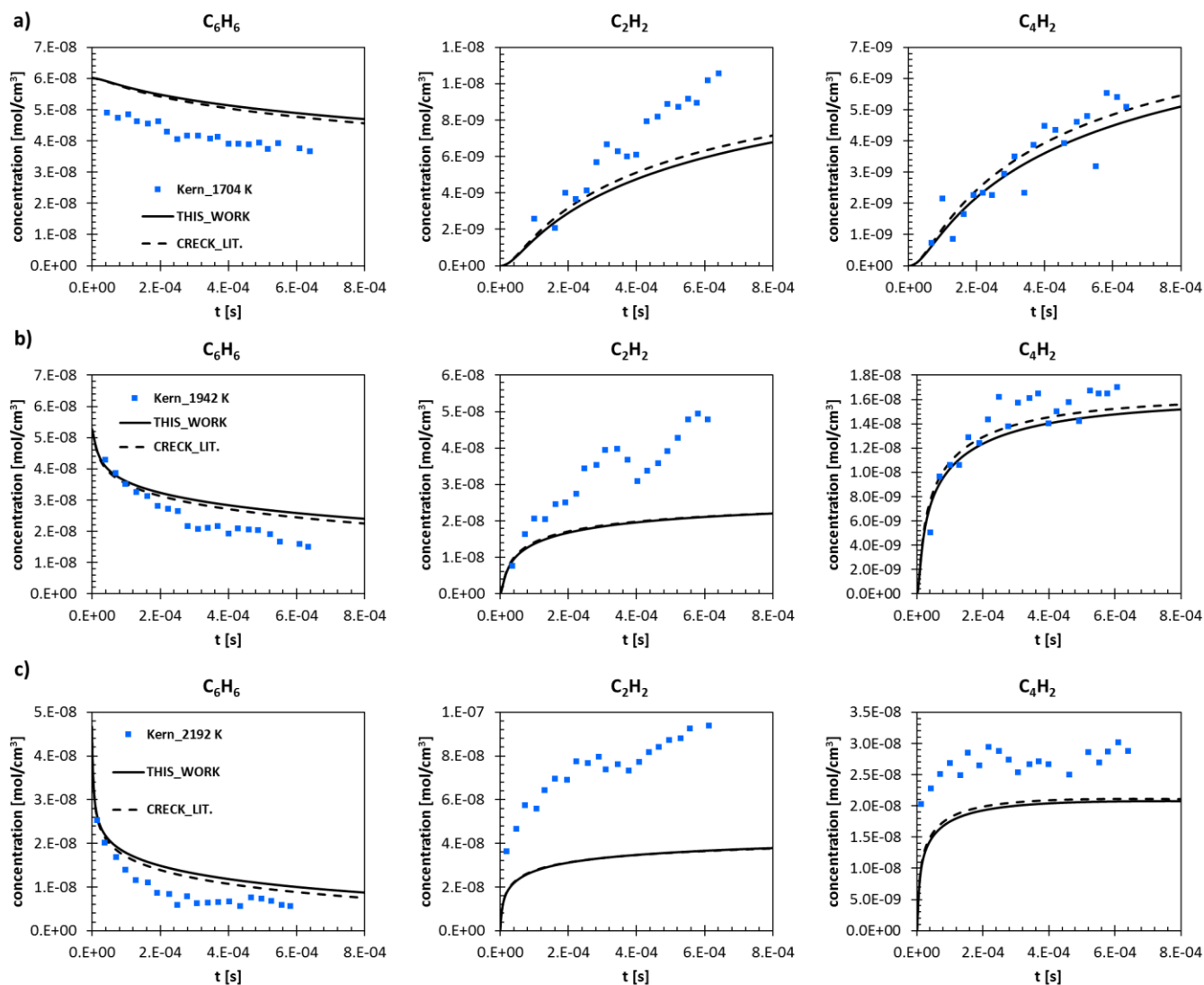
Figure S3: Species profiles of the Shock tube experiments of Kern et al.[11] (0.2-3 atm, 1515-2500 K), at different temperatures (a) 1704 K, b) 1942 K, c) 2192 K).
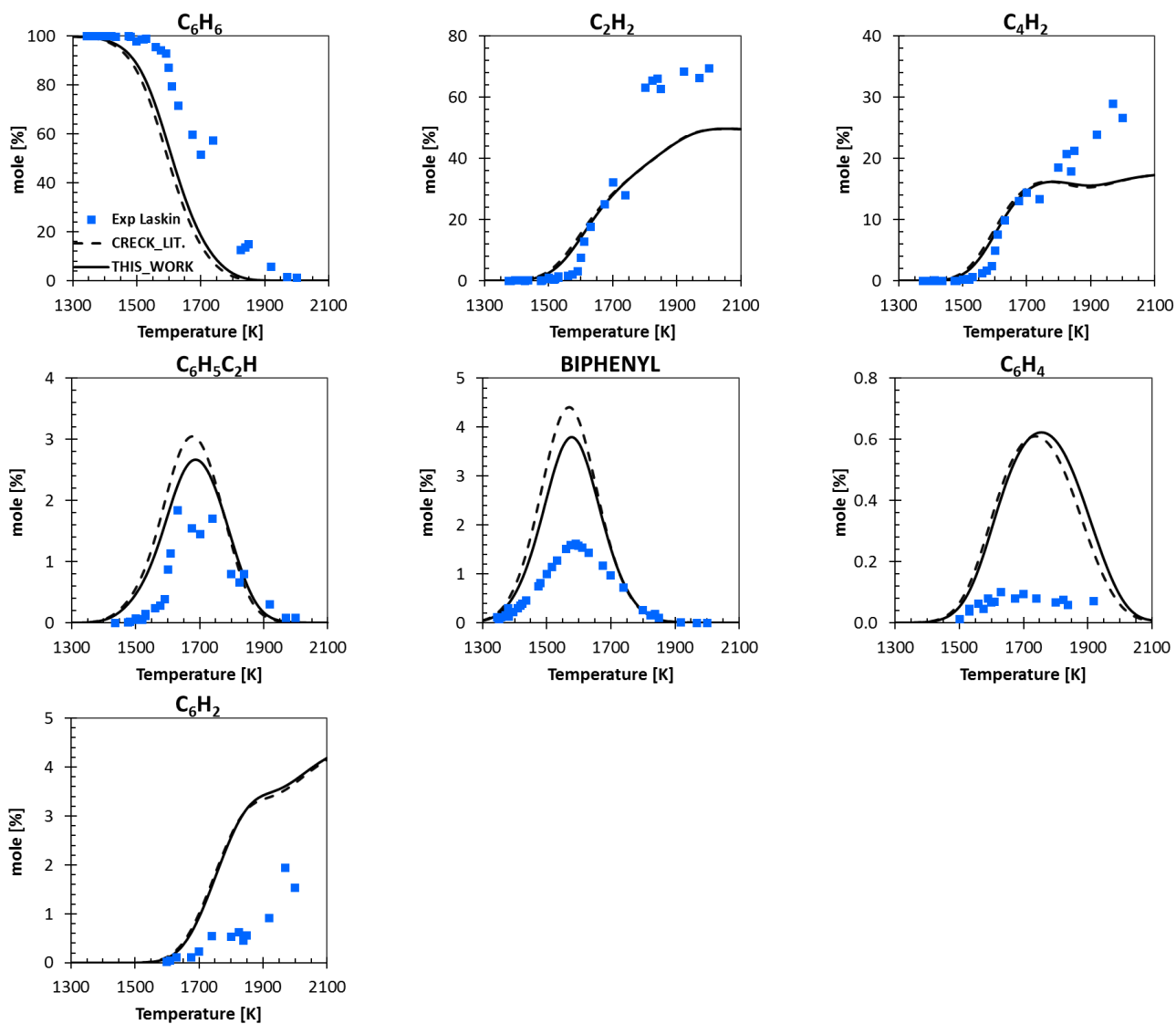
Figure S4: Species profiles of the ST reactor experiments of Laskin et al.[12] (1300 K, 5 atm)
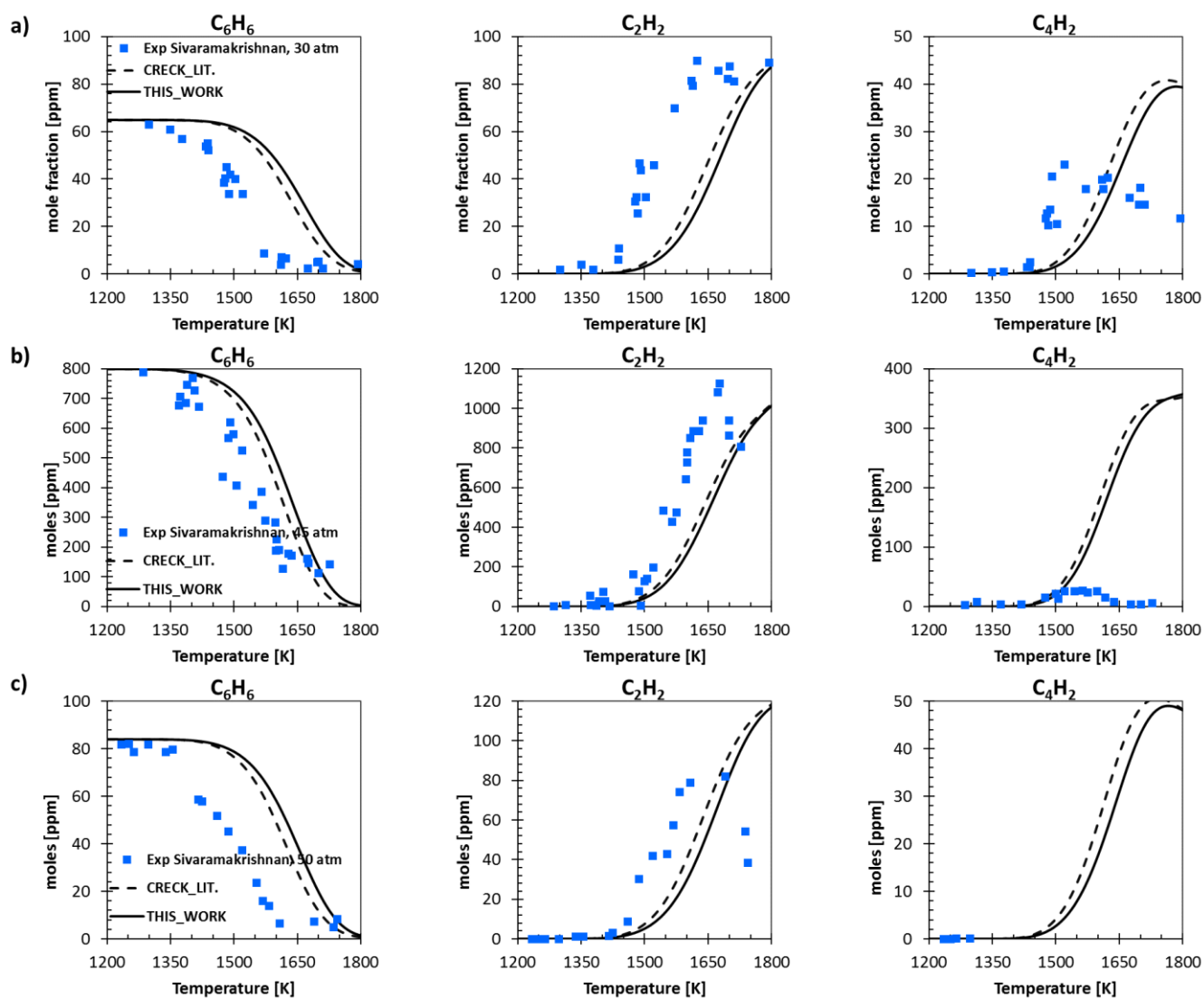
Figure S5: Species profiles of the ST experiments of Sivaramakrishnan et al. 30, 45 and 50 atm (a, b, c, respectively).[13]

Oxidation
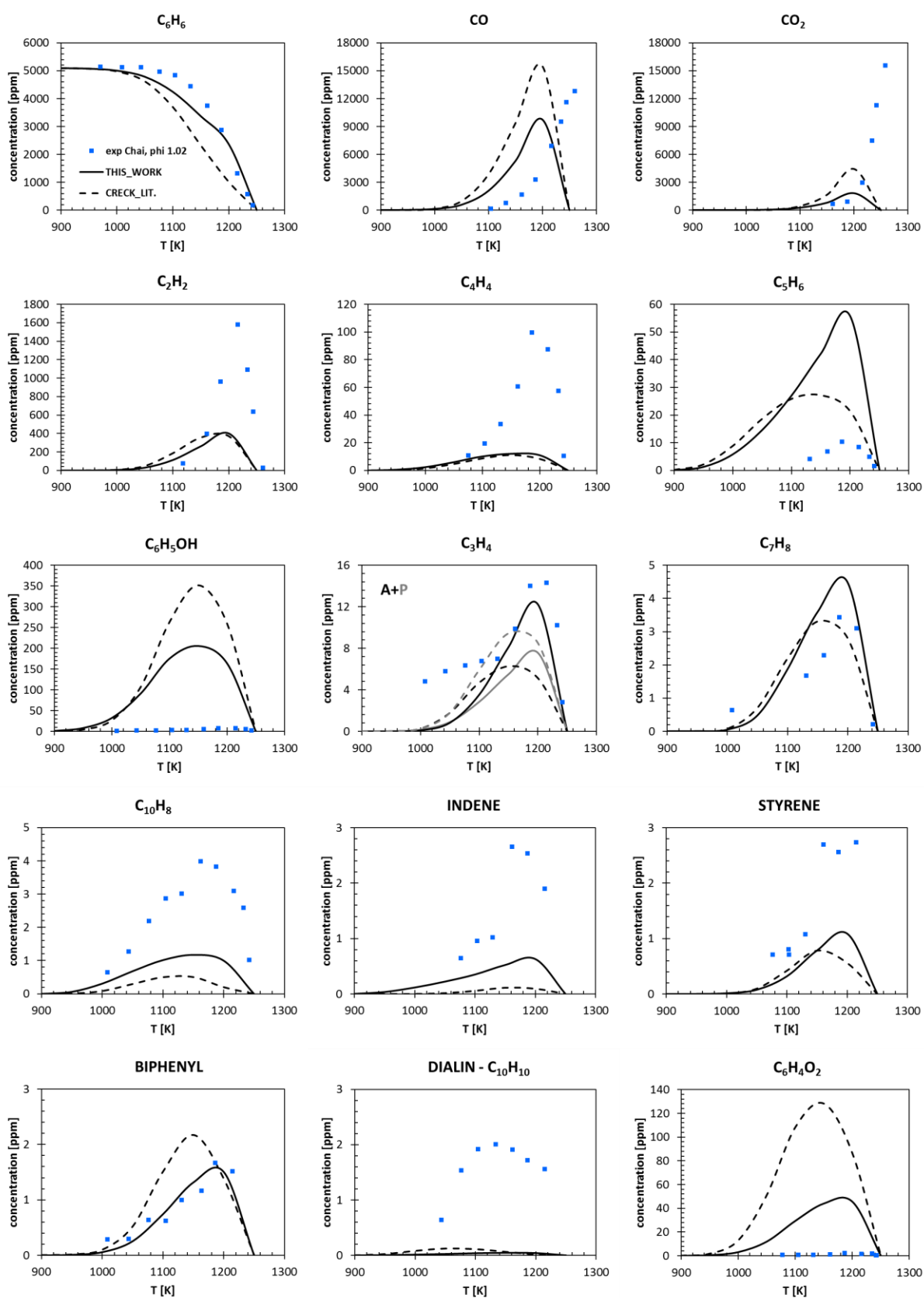
Figure S6: Species profiles in the Jet Stirred Reactor of Chai et al., at 0.46 atm, phi = 1.02[14]

9
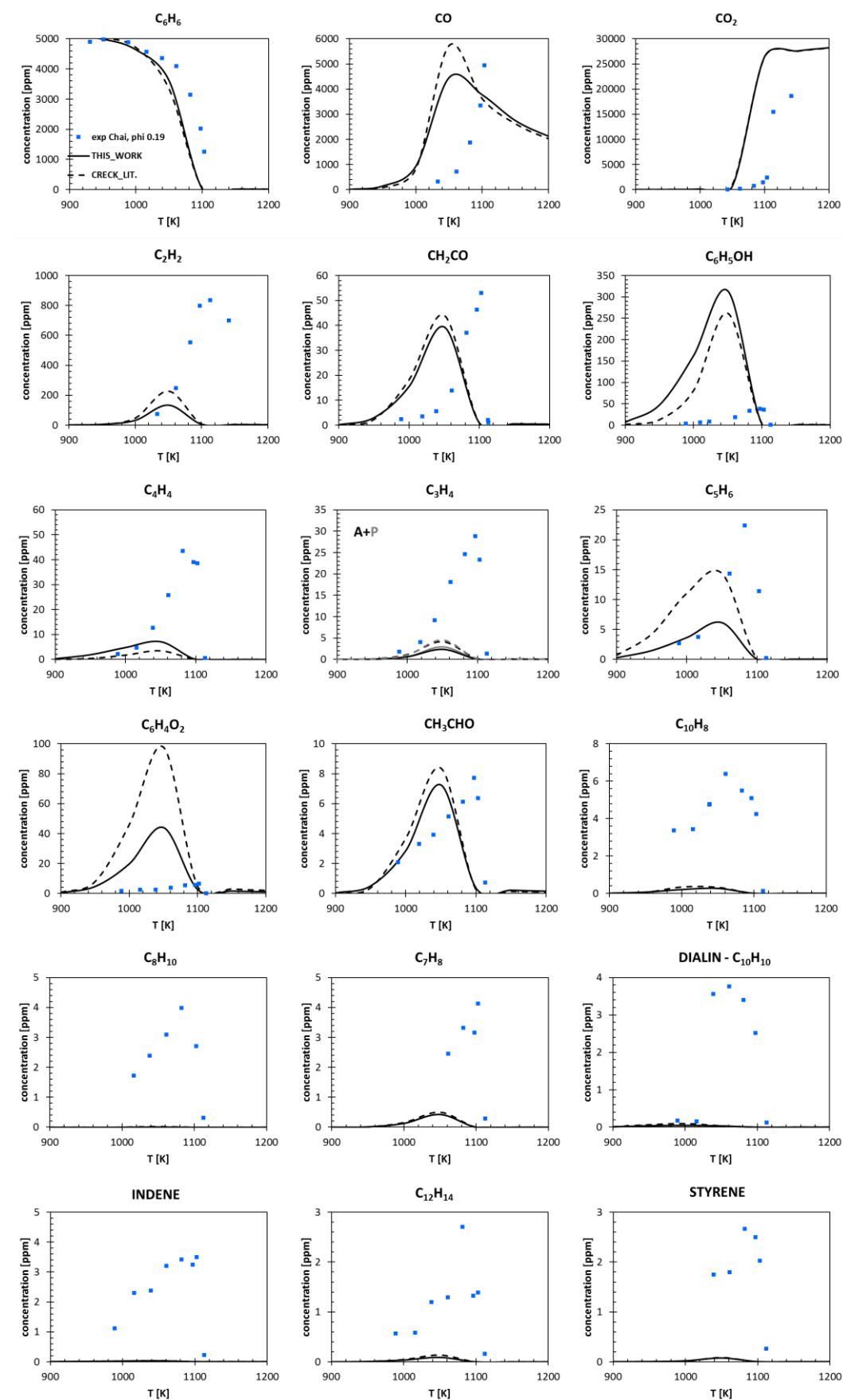
Figure S7: Species profiles in the Jet Stirred Reactor of Chai et al., at 0.46 atm, phi = 0.19[14]
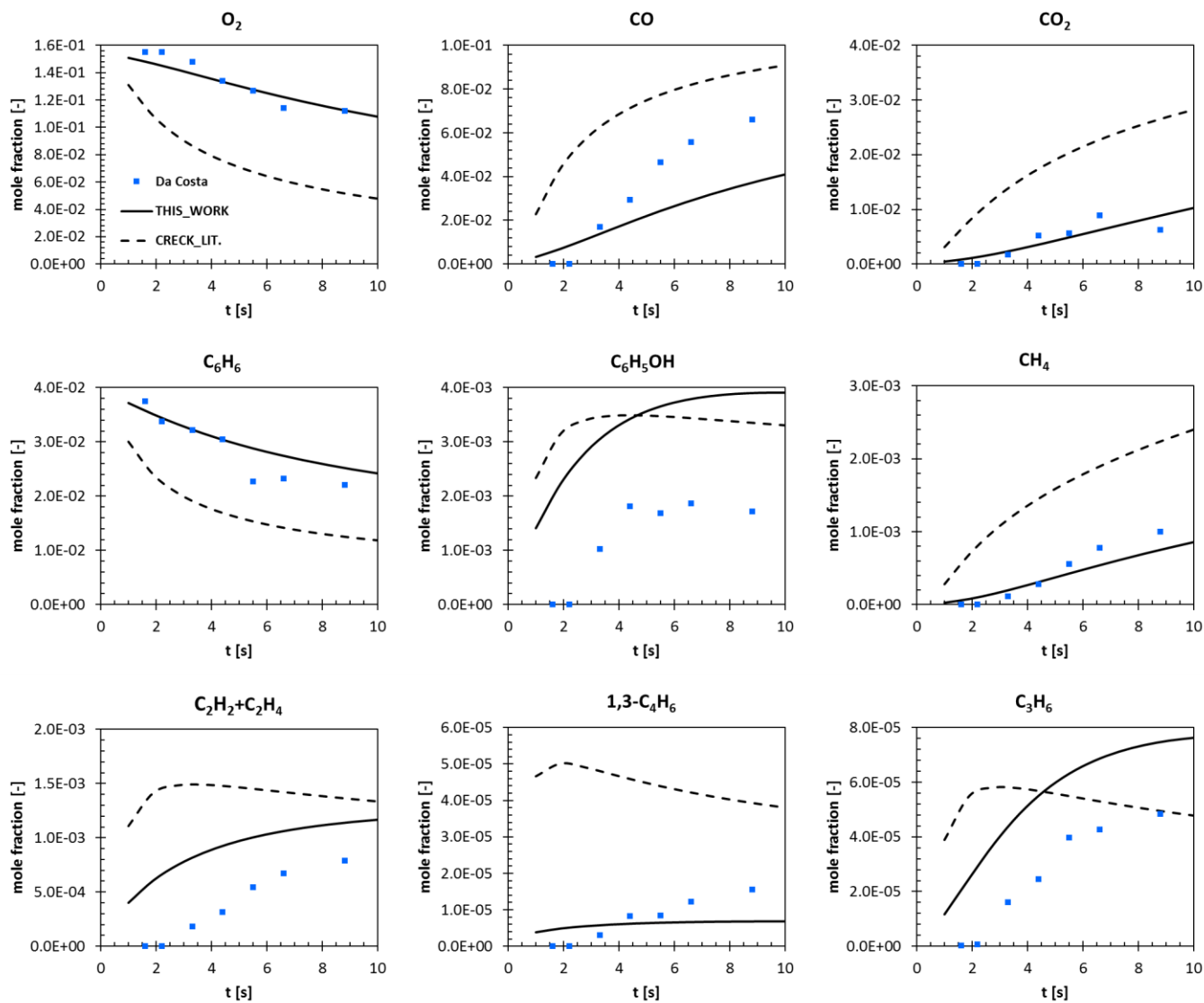
Figure S8: Species profiles of the Jet Stirred Reactor experiments of Da Costa et al., at 923 K, 1 atm, phi = 1.9[15]
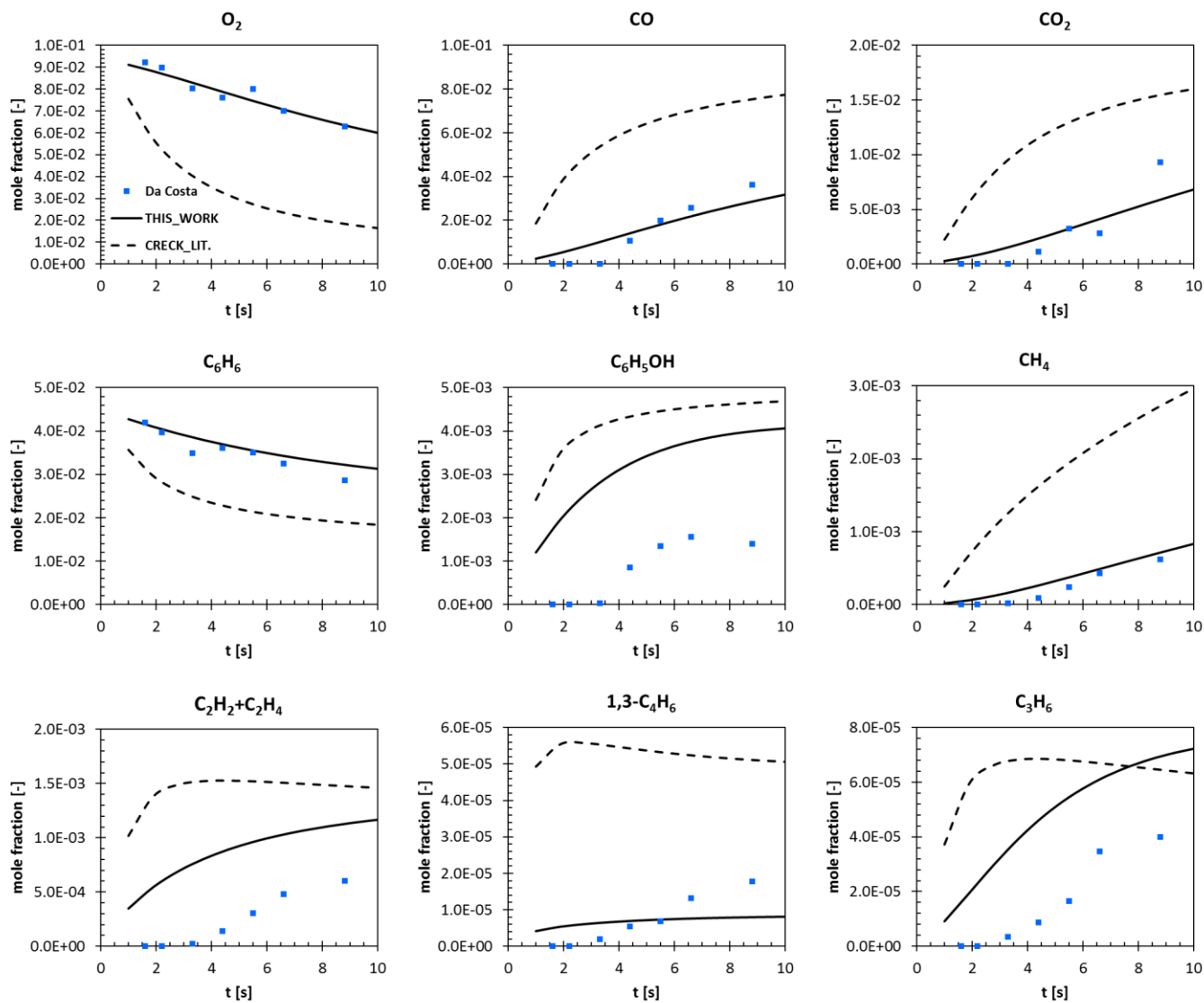
Figure S9: Species profiles of the Jet Stirred Reactor experiments of Da Costa et al., at 923 K, 1 atm, phi = 3.6[15]
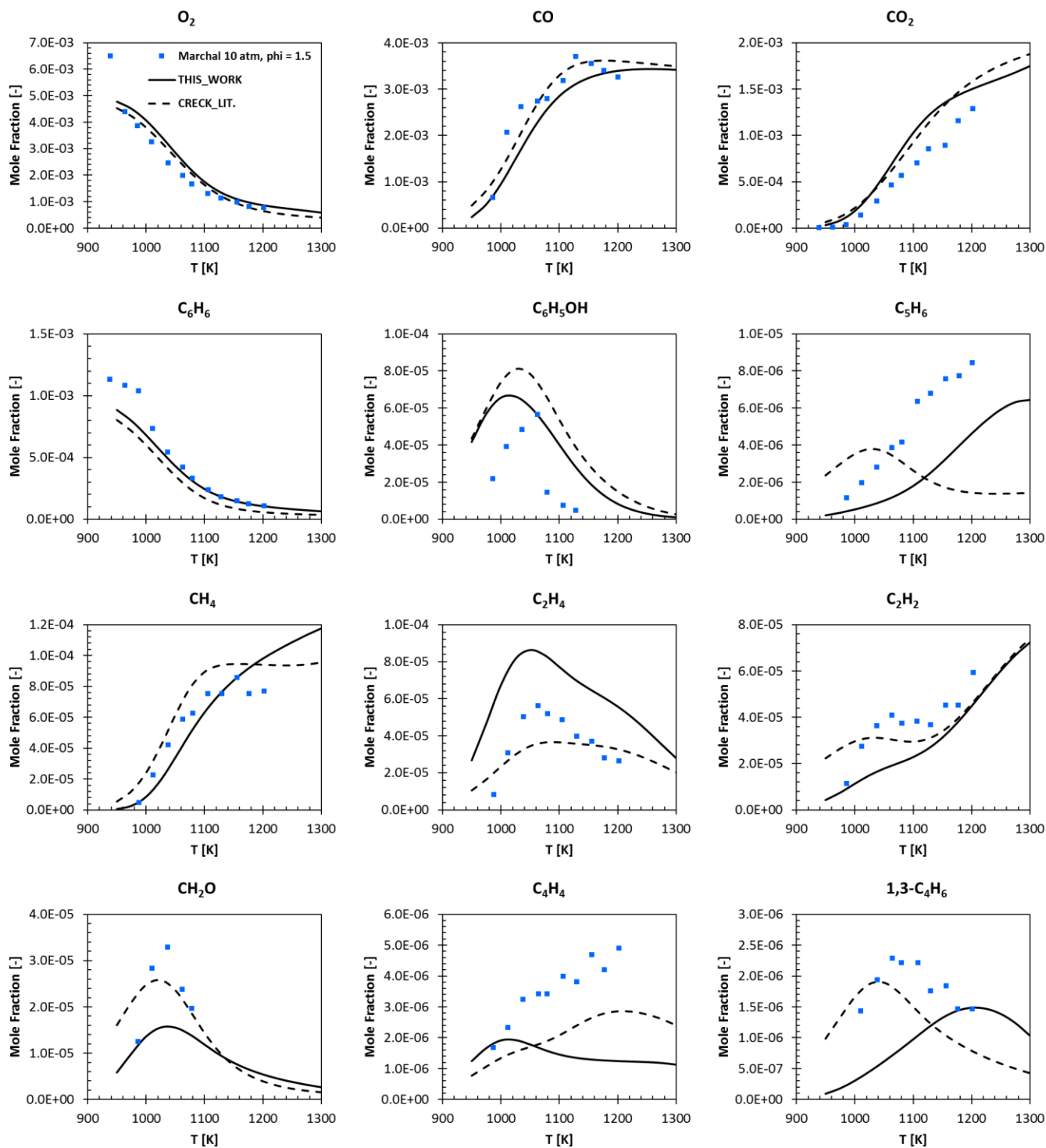
Figure S10: Species profiles of the jet stirred reactor experiments of Marchal et al. (10 atm, phi = 1.5)[16]

13
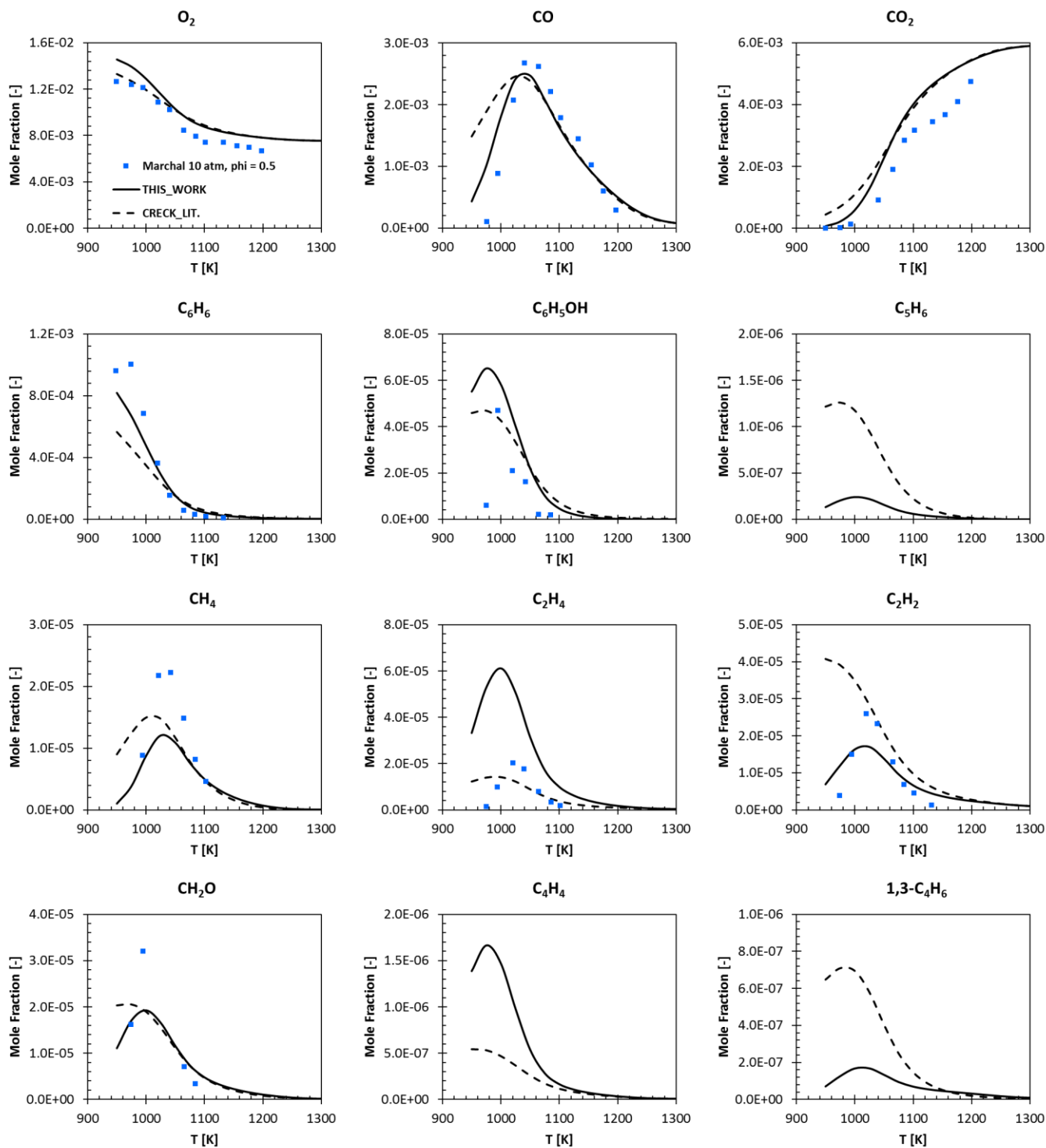
Figure S11: Species profiles of the jet stirred reactor experiments of Marchal et al. (10 atm, phi = 0.5)[16]
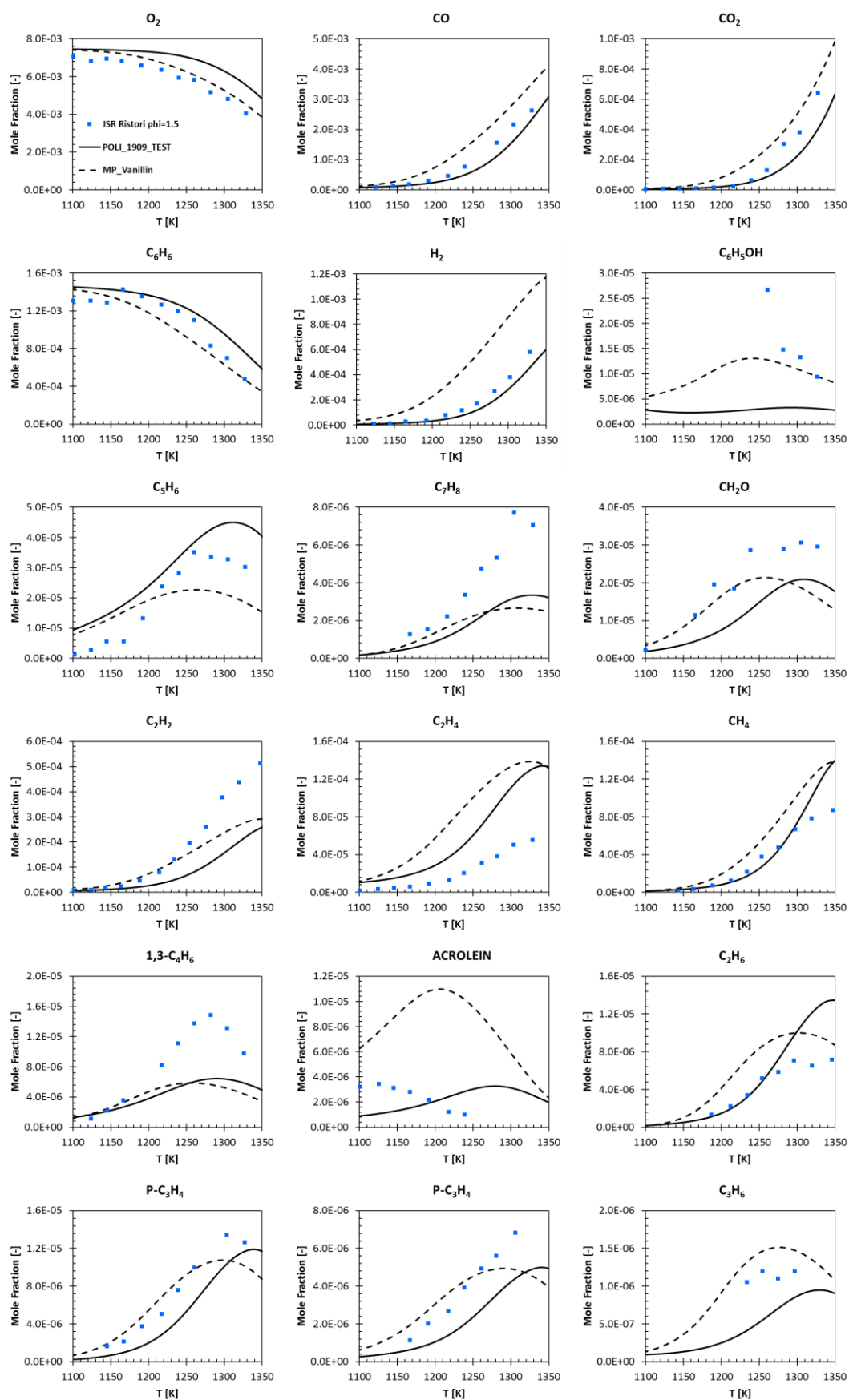
Figure S12: Profiles of the jet stirred reactor experiments of Ristori et al. (1 atm, phi = 1.5)[17]
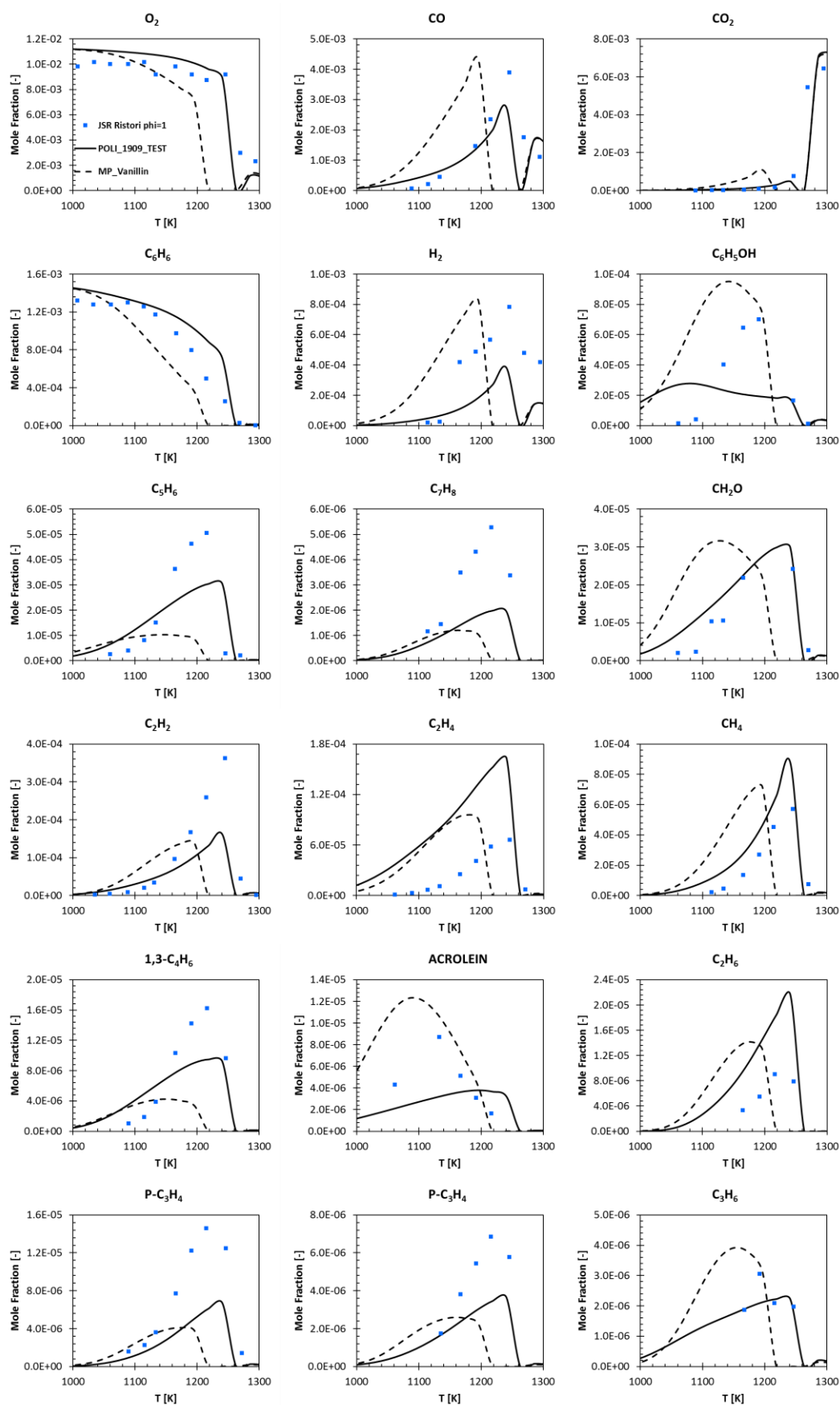
Figure S13: Profiles of the jet stirred reactor experiments of Ristori et al. (1 atm, phi = 1.0)[17]
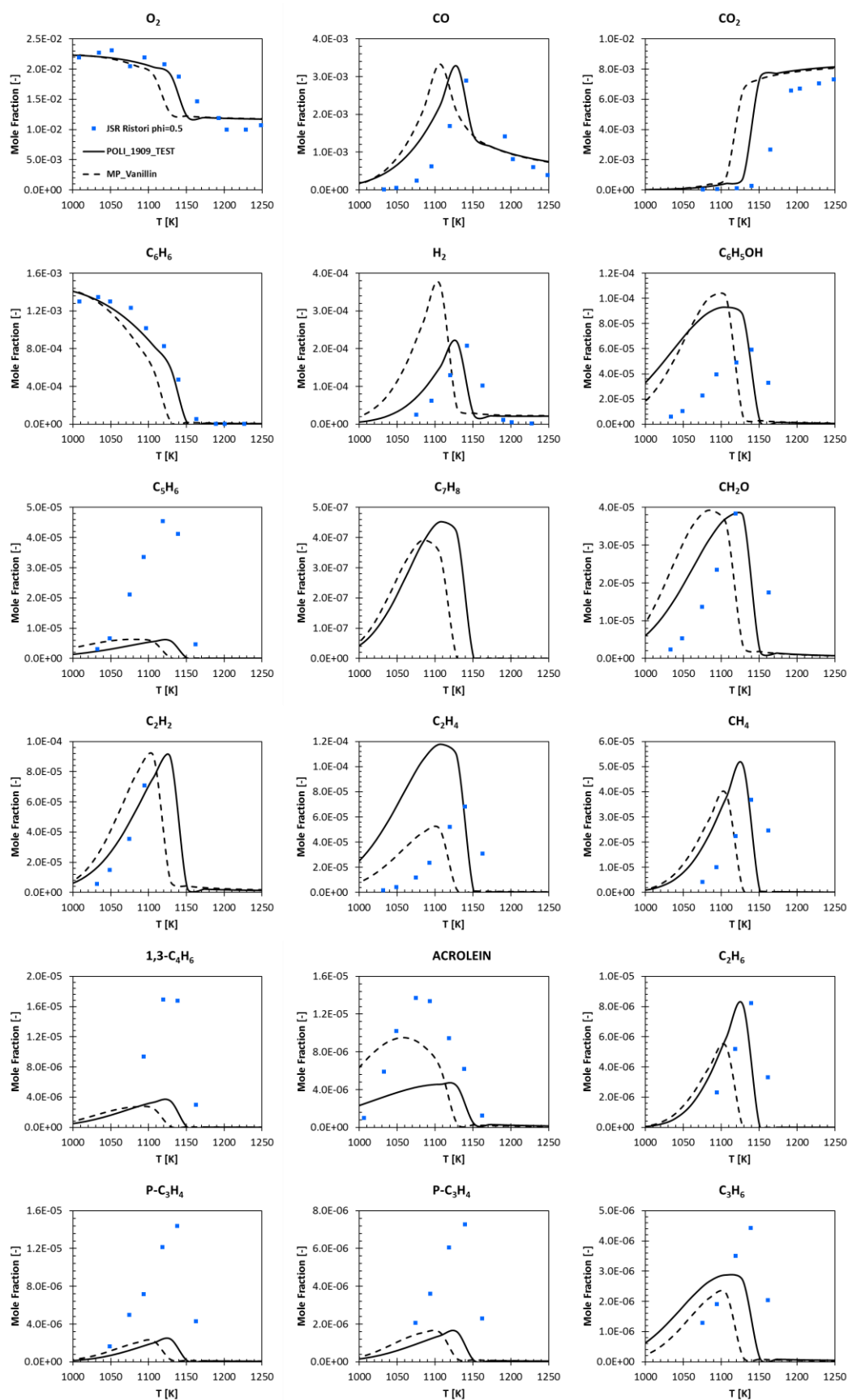
Figure S14: Profiles of the jet stirred reactor experiments of Ristori et al. (1 atm, phi = 0.5)[17]
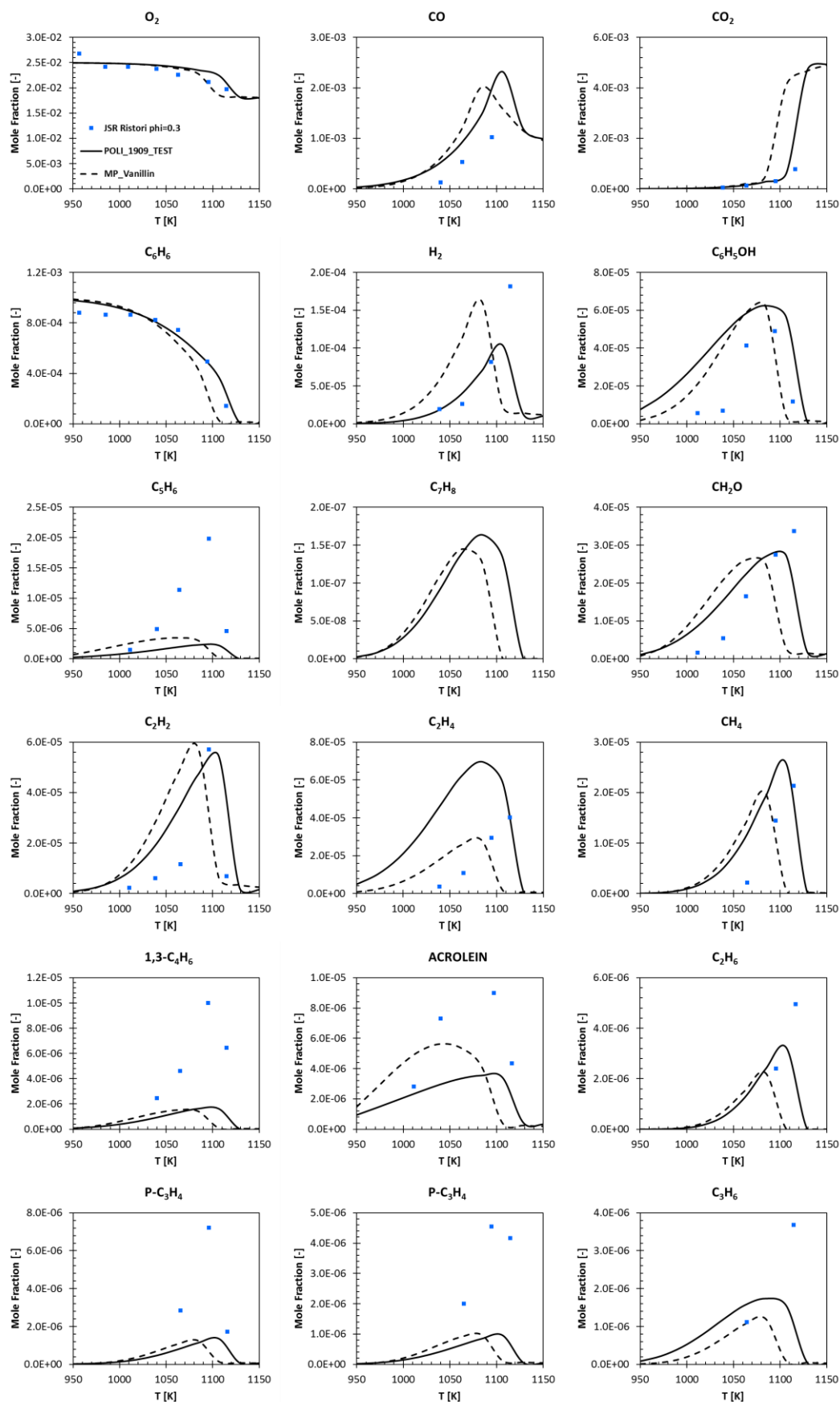
Figure S15: Profiles of the jet stirred reactor experiments of Ristori et al. (1 atm, phi = 0.3)[17]
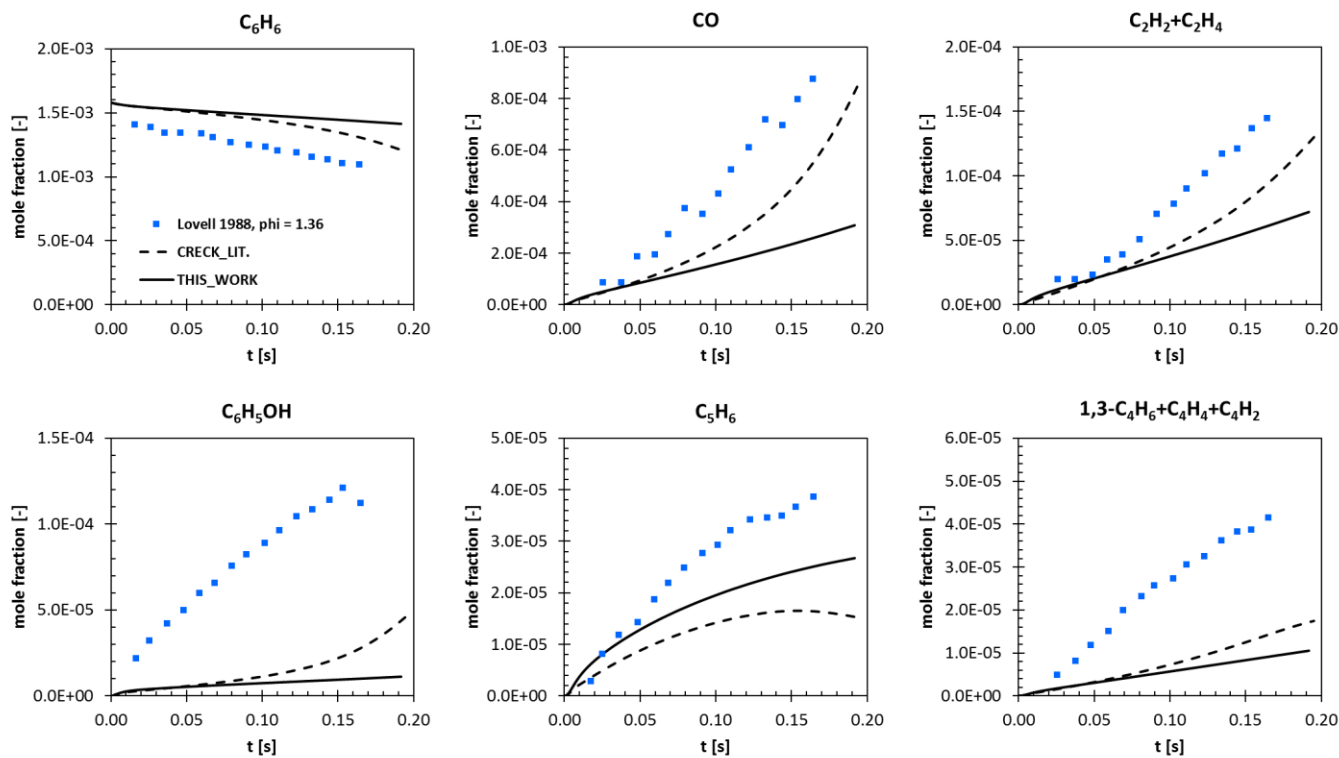
Figure S16: Species profiles of the plug flow reactor experiments of Lovell et al. (1102 K, 1 atm, phi = 1.36)[18]
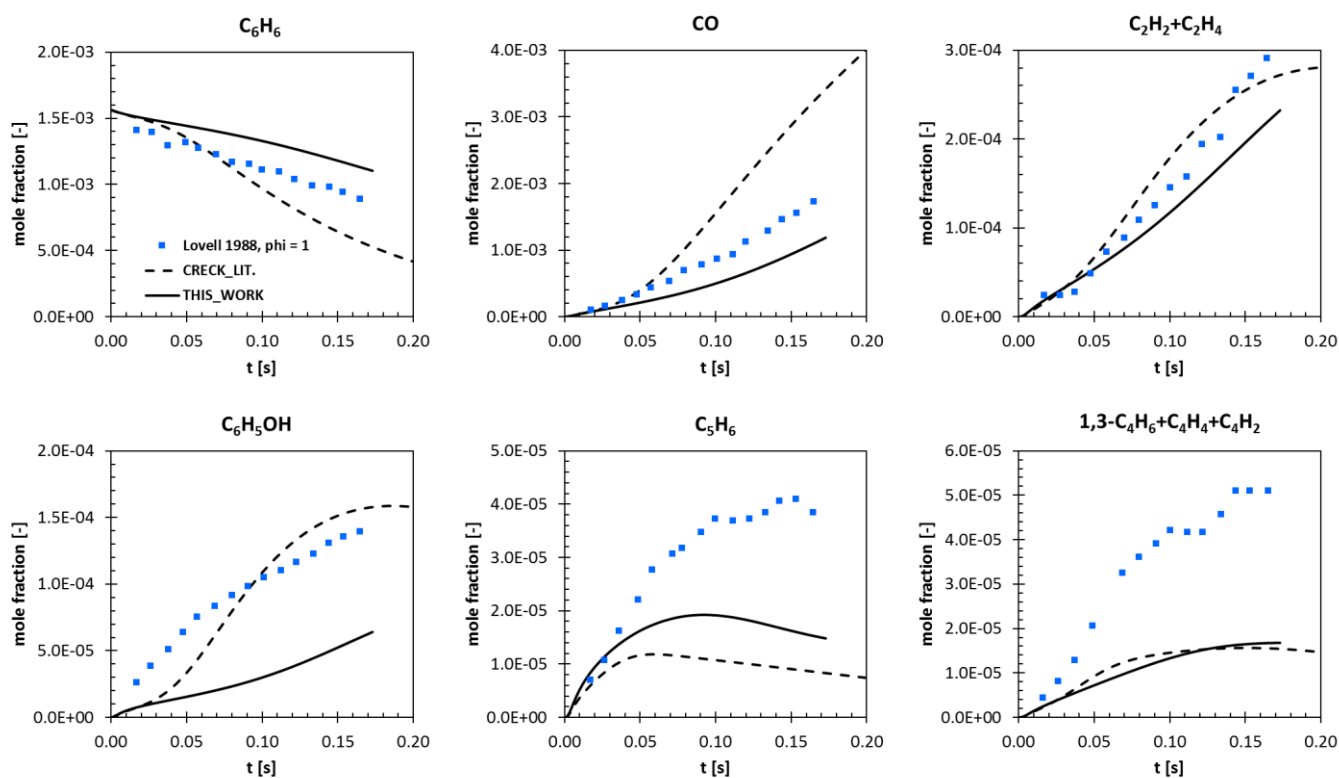
Figure S17: Species profiles of the plug flow reactor experiments of Lovell et al. (1102 K, 1 atm, phi = 1)[18]

19
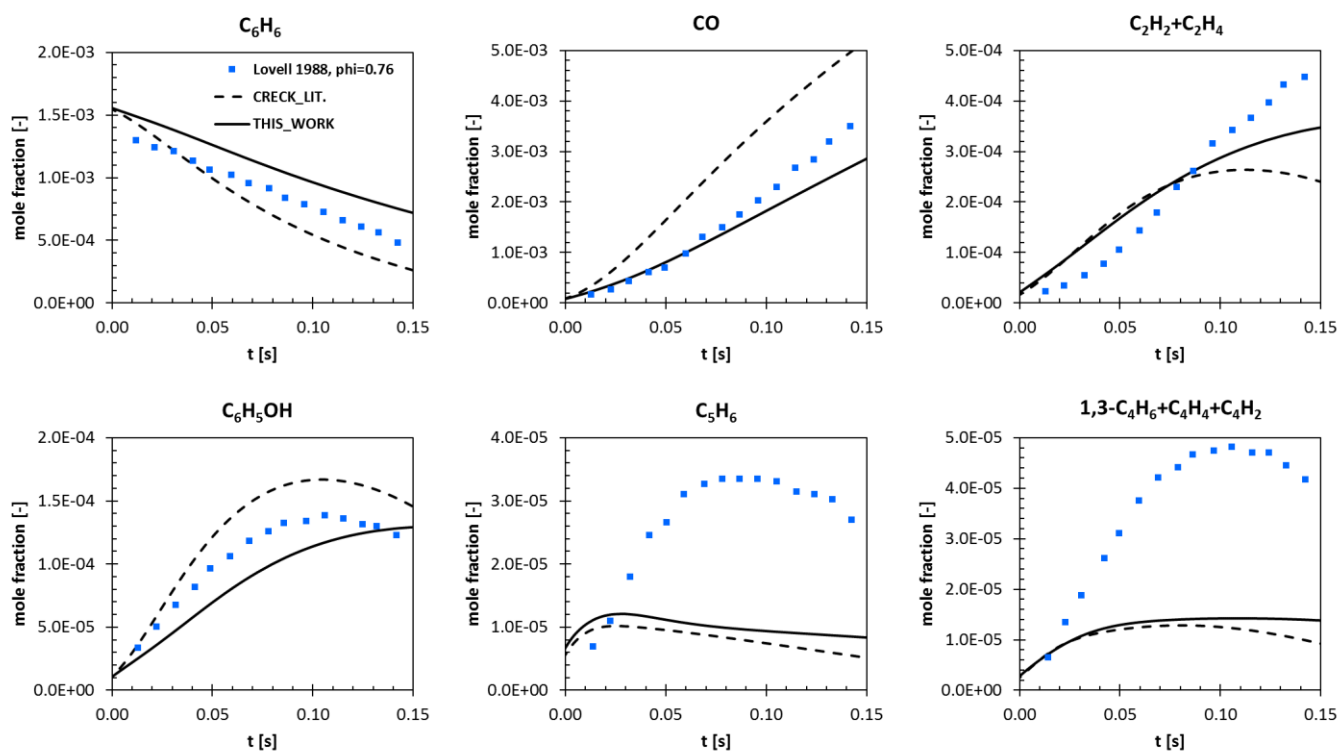
Figure S18: Species profiles of the plug flow reactor experiments of Lovell et al. (1102 K, 1 atm, phi = 1)[18]
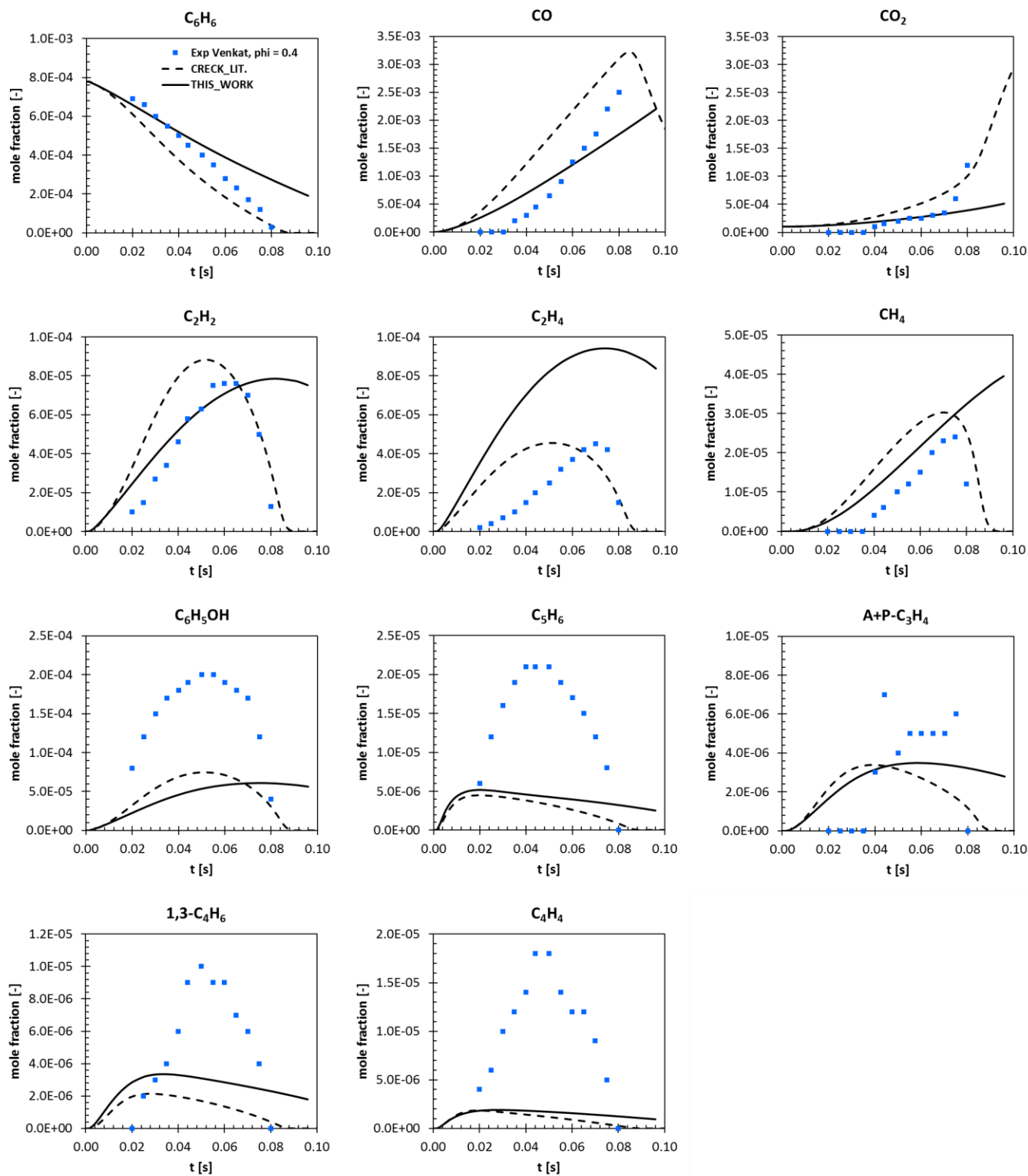
Figure S19: Species profiles of the plug flow reactor experiments of Venkat et al. (1120 K, 1 atm, phi = 0.4)[19]
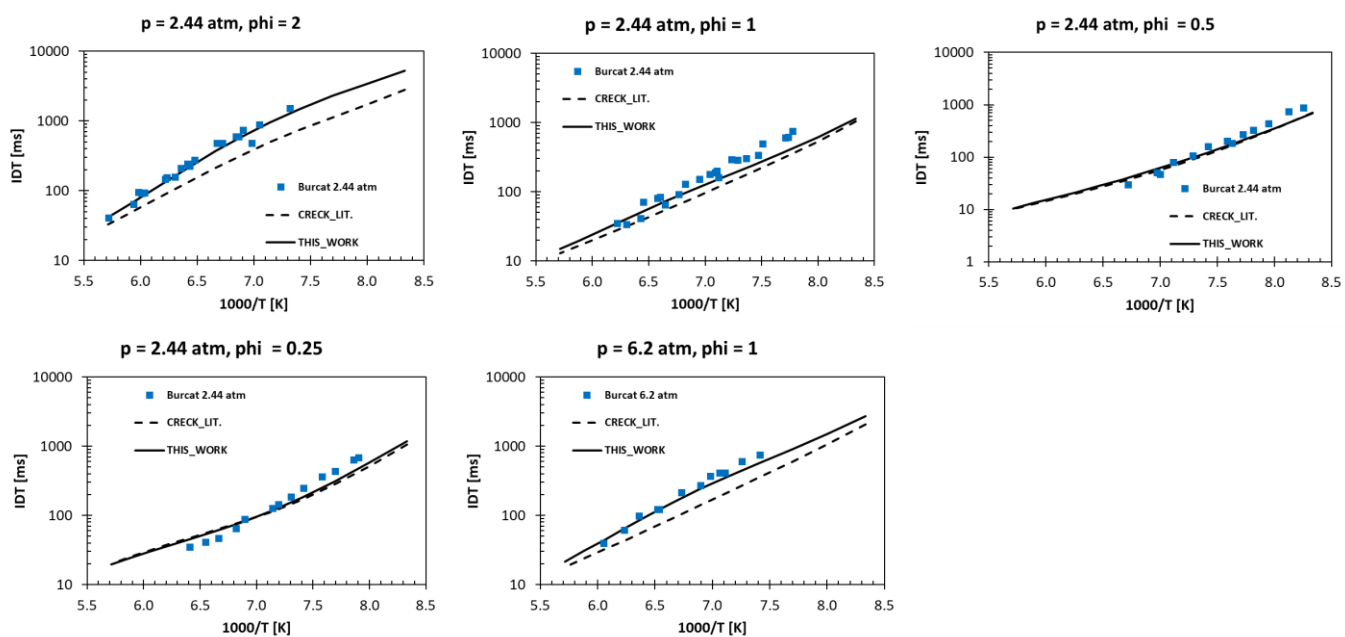
Figure S20: Ignition delay time measures of the shock tube experiments of Burcat et al. Operating conditions are indicated on the plots.[20]
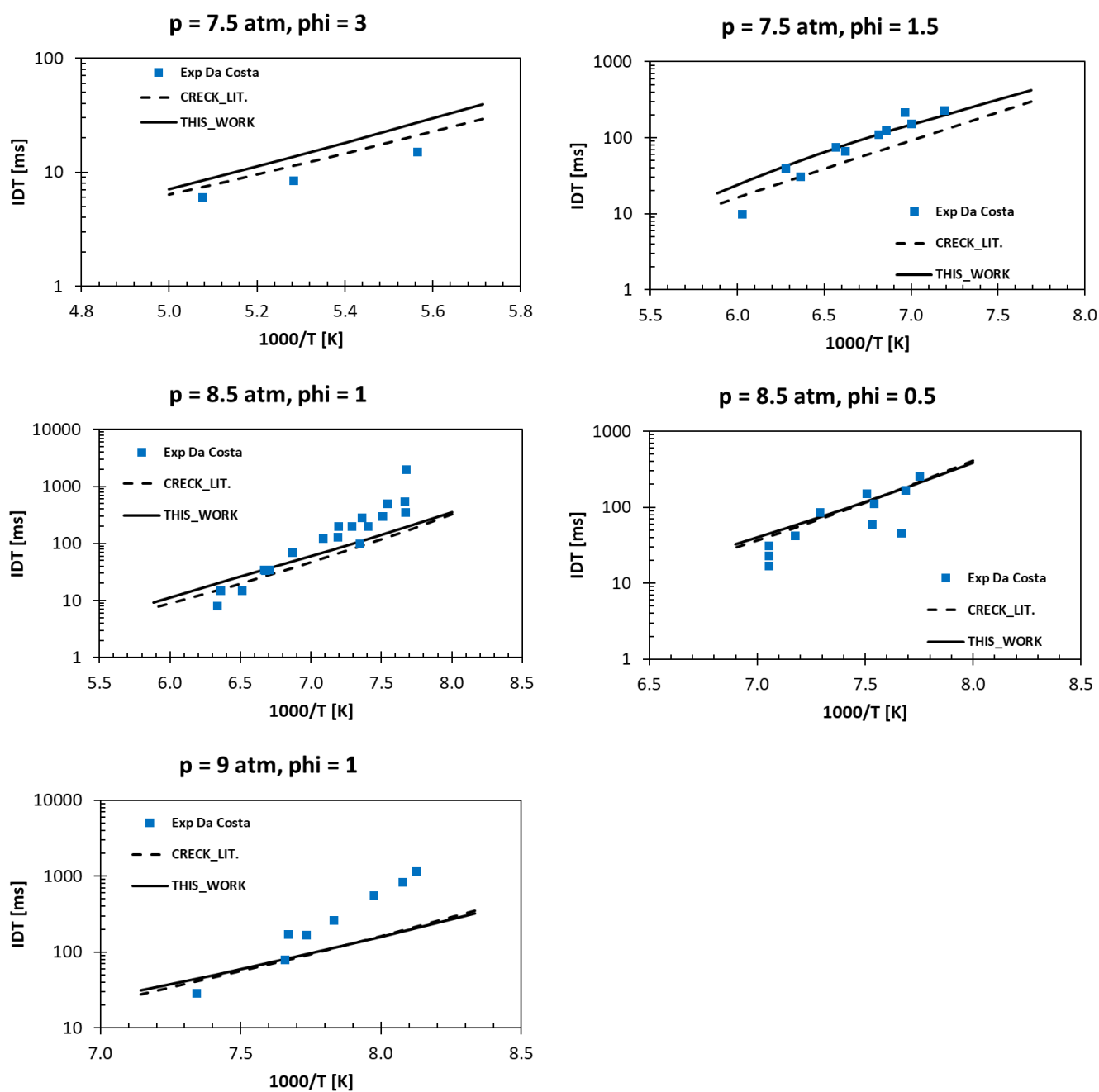
Figure S21: Ignition delay time measures of the shock tube experiments of Da Costa et al.[15] Operating conditions are indicated on the plots.
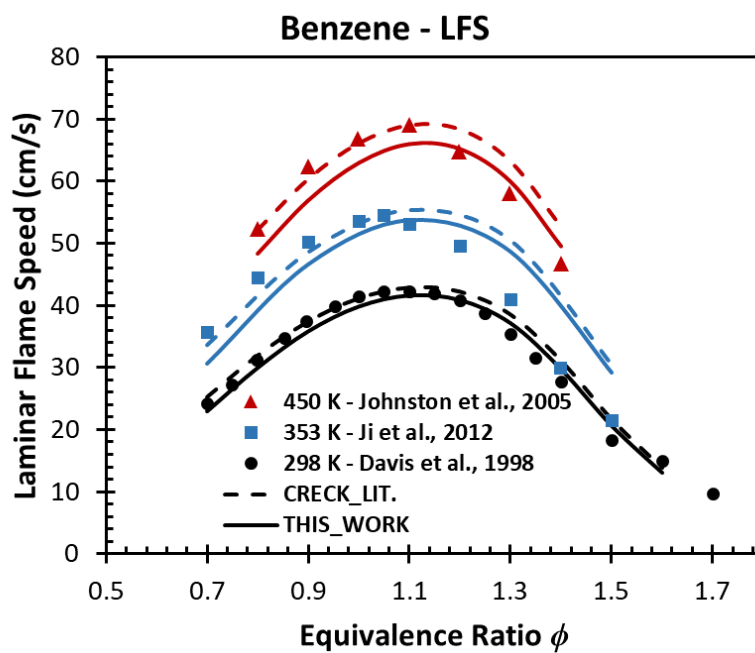
Figure S22: Laminar flame speed of benzene.[21–23]

c) Cyclopentadiene pyrolysis and oxidation

Pyrolysis
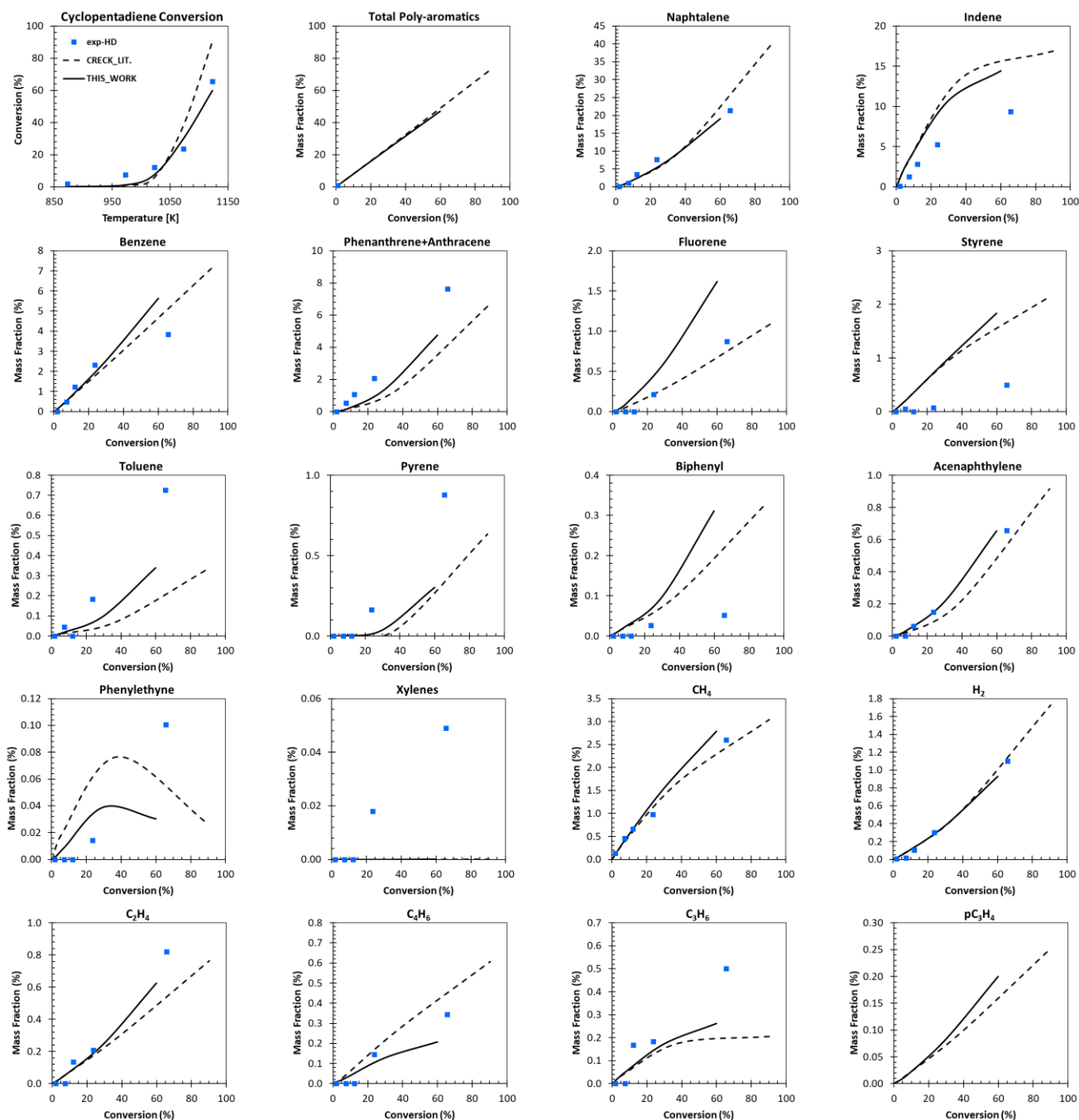
Figure S23: Species profiles of the plug flow reactor of Djokic et al. (1.7 atm), at high dilution conditions.[24]
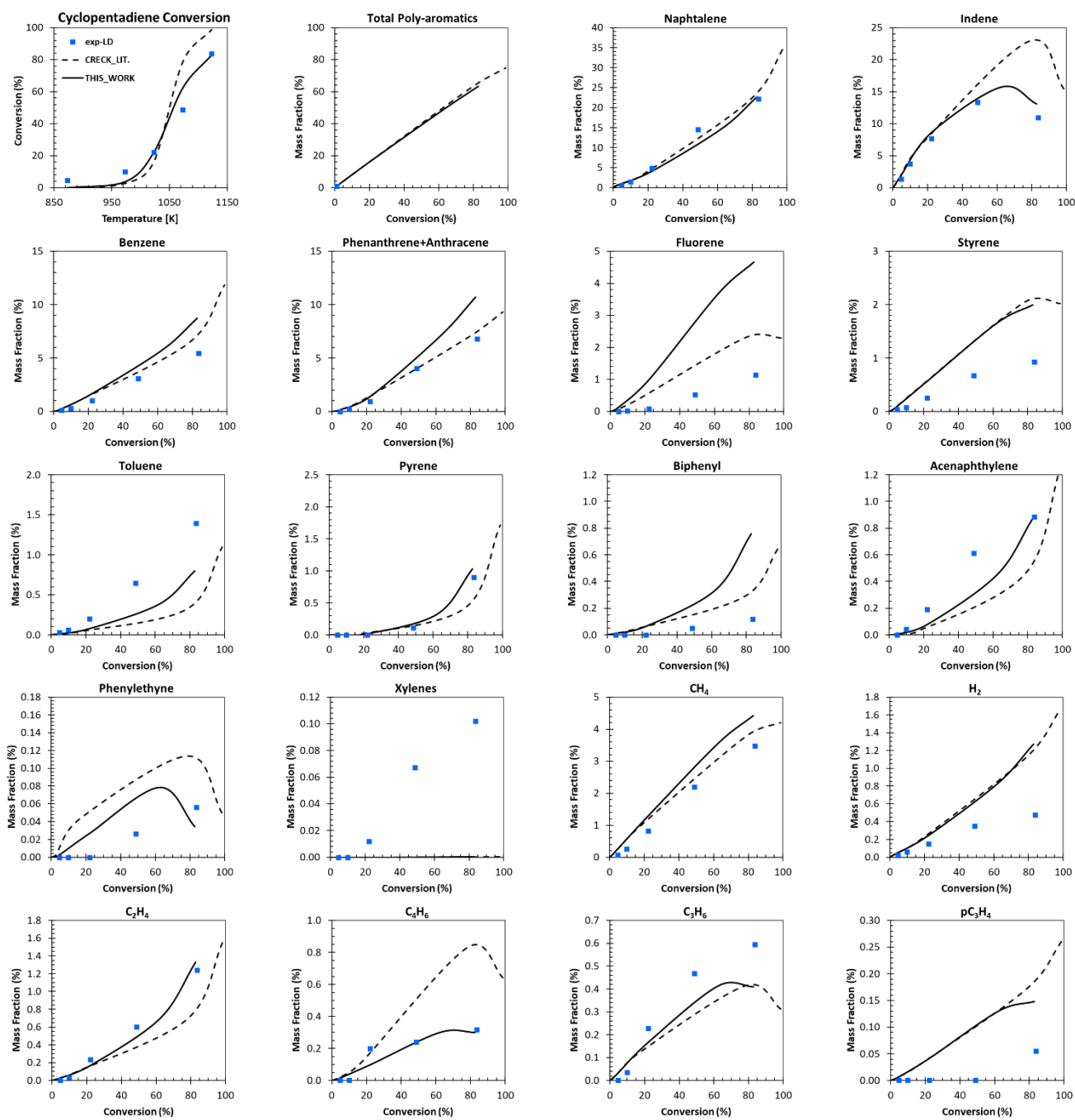
Figure S24: Species profiles of the plug flow reactor of Djokic et al. (1.7 atm), at low dilution conditions.[24]
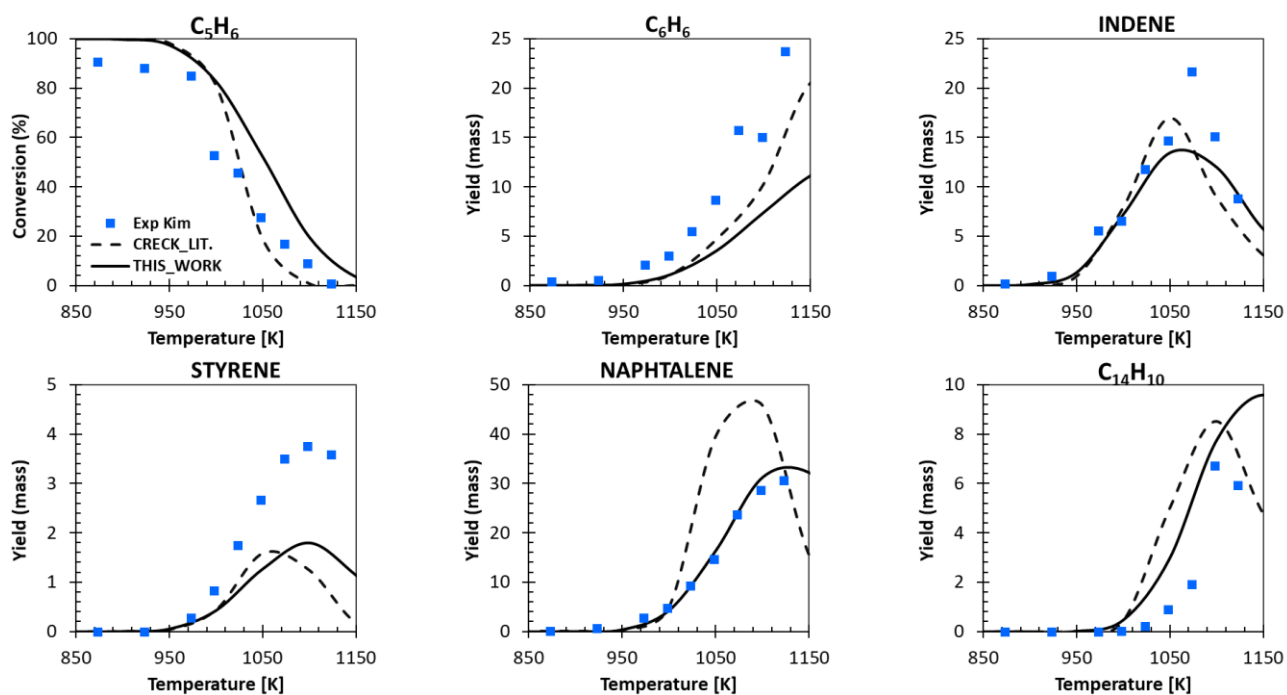
Figure S25: Species profiles of the plug flow reactor experiments of Kim et al.[25]
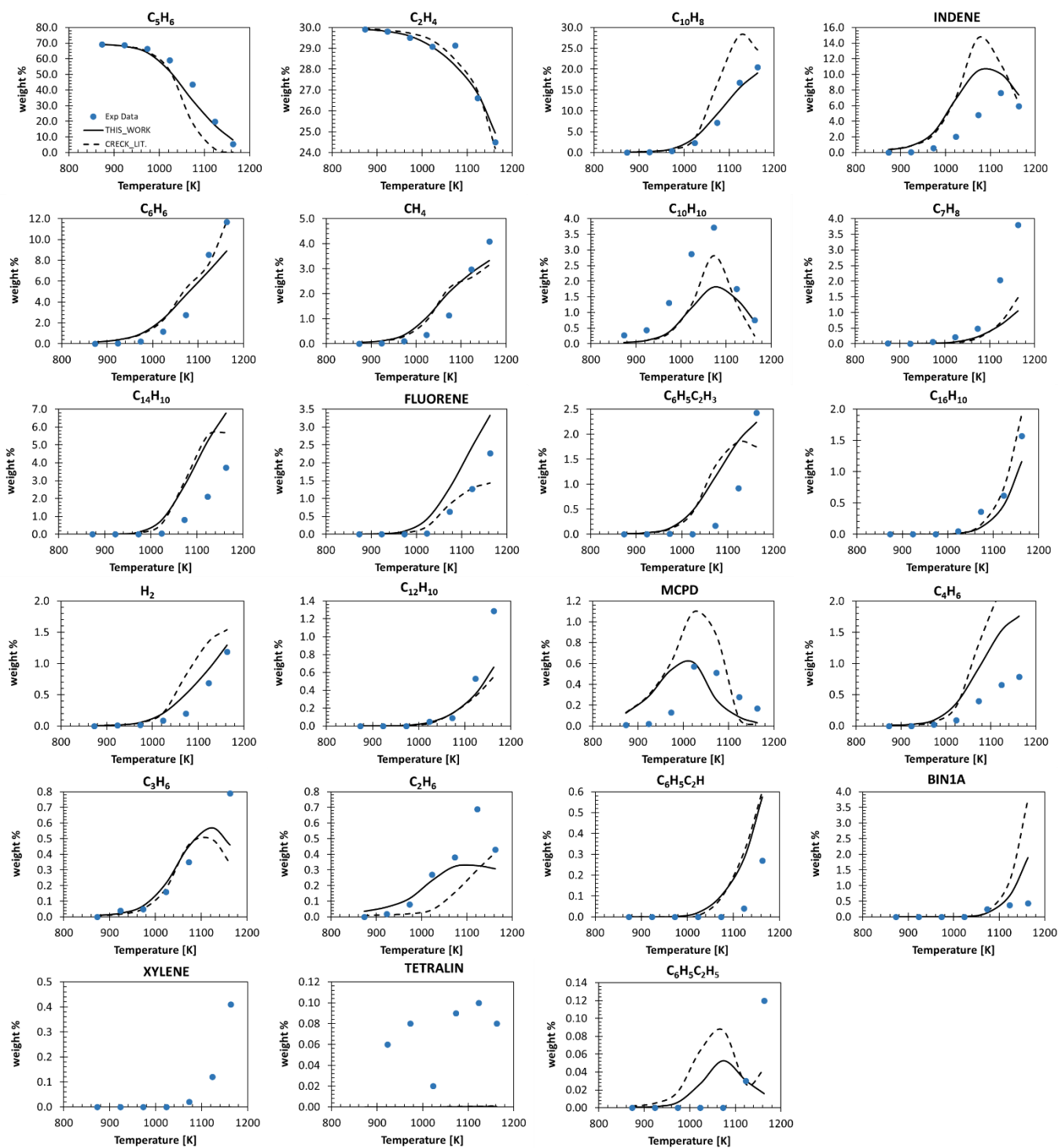
Figure S26: Species profiles of the plug flow reactor experiments of Vervust et al.[26]

Oxidation
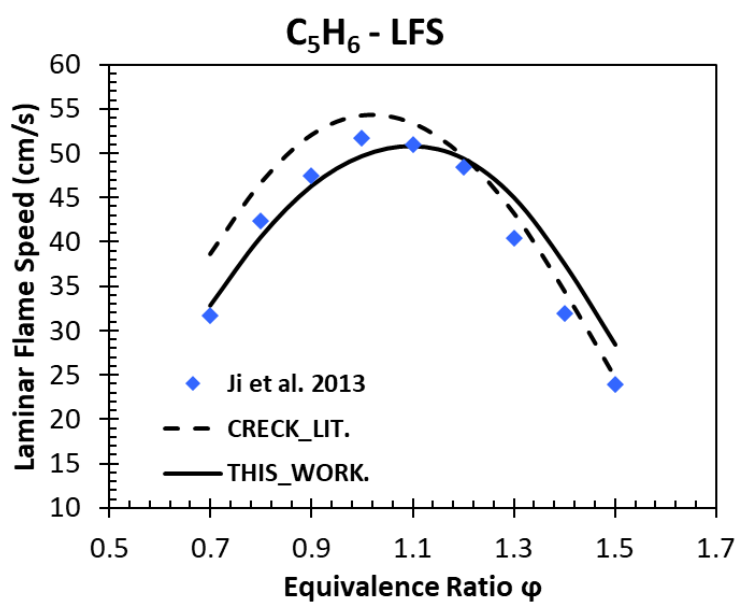
Figure S27: Laminar flame speeds of cyclopentadiene.[27]
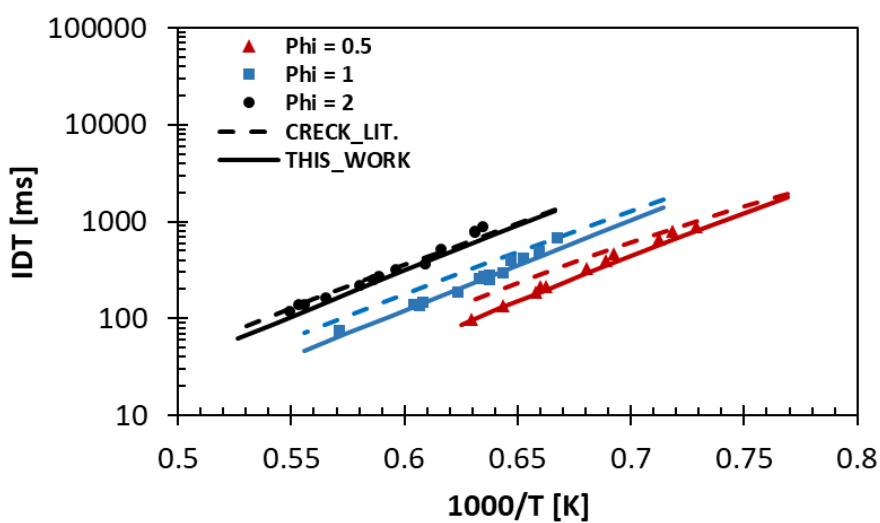
Figure S28: Ignition delay times of cyclopentadiene measured in the shock tube reactor of Orme et al.[28]
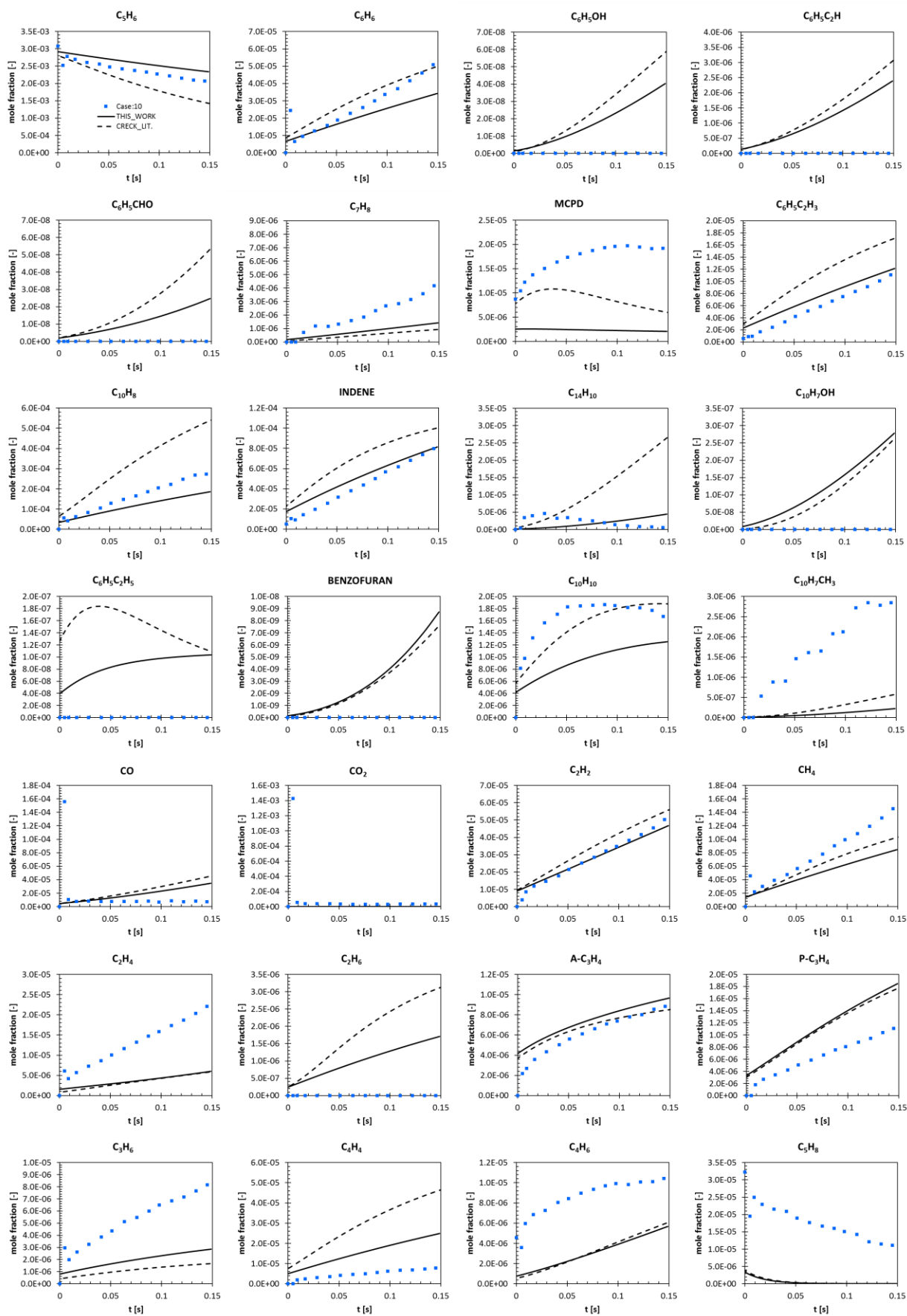
Figure S29: Species profiles in the plug flow reactor experiments of Butler et al. (T = 1150 K, P = 1 atm, phi = 150)[29]
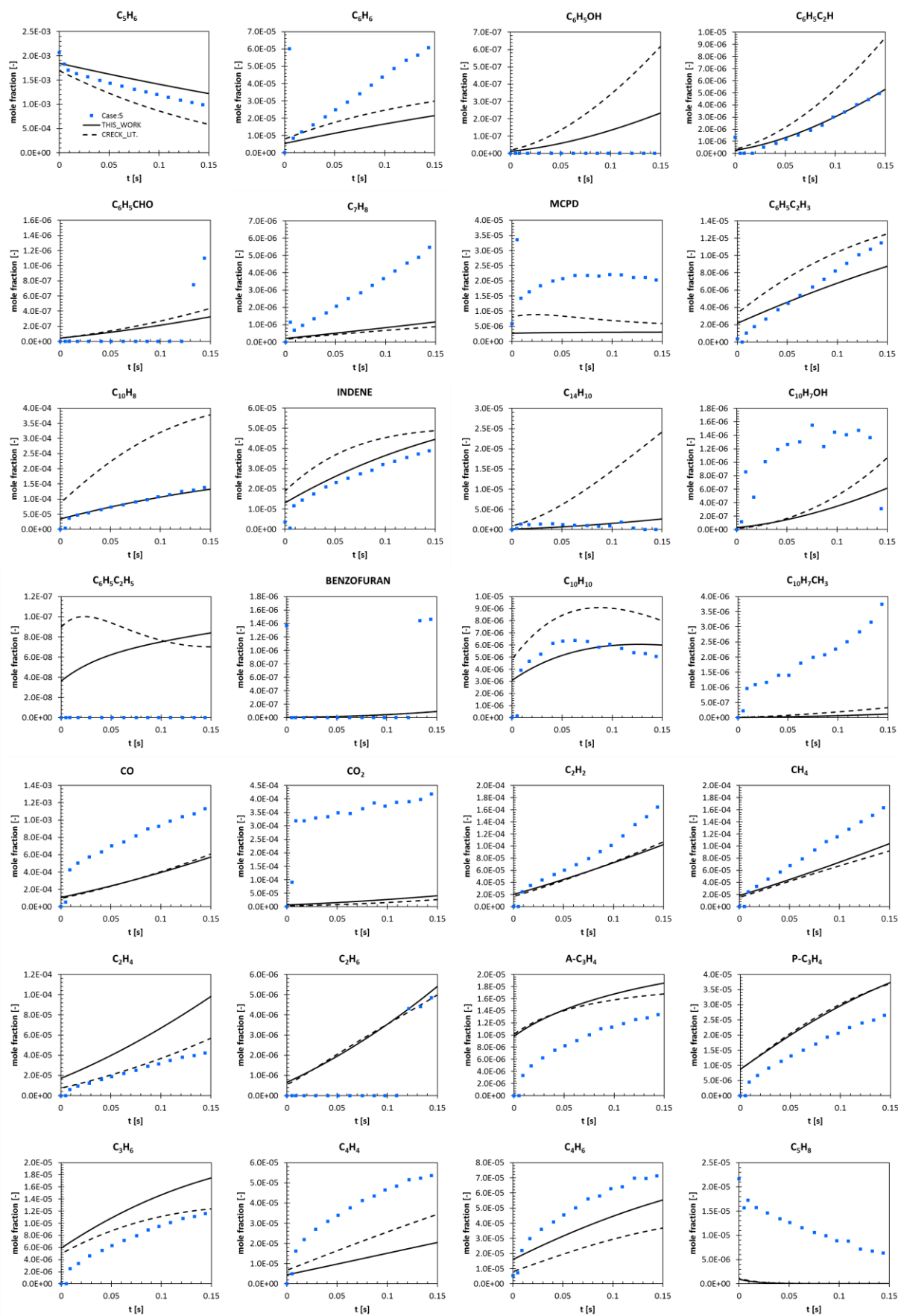
Figure S30: Species profiles in the plug flow reactor experiments of Butler et al. (T = 1150 K, P = 1 atm, phi = 1.61)[29]
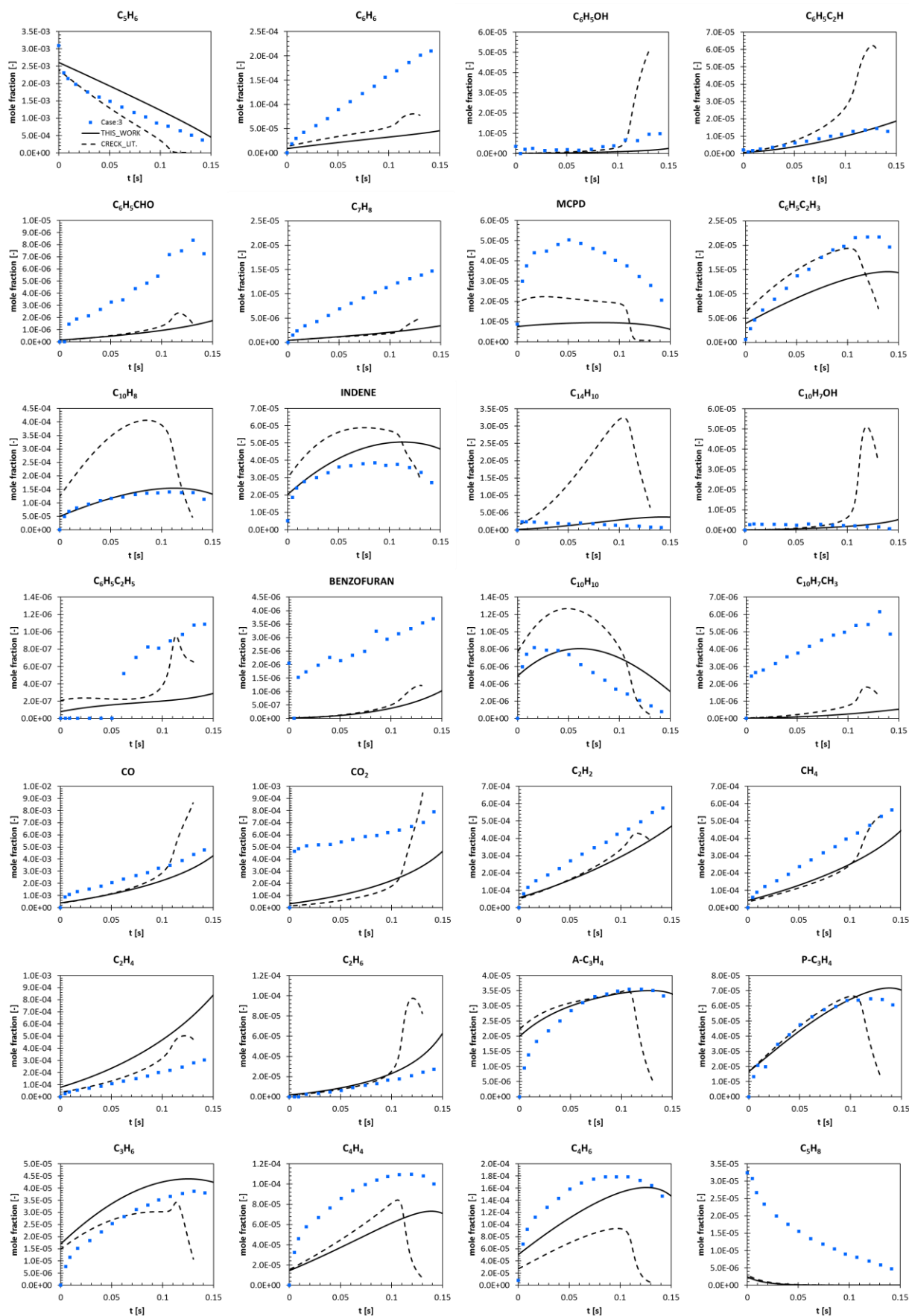
Figure S31: Species profiles in the plug flow reactor experiments of Butler et al. (T = 1150 K, P = 1 atm, phi = 1)[29]
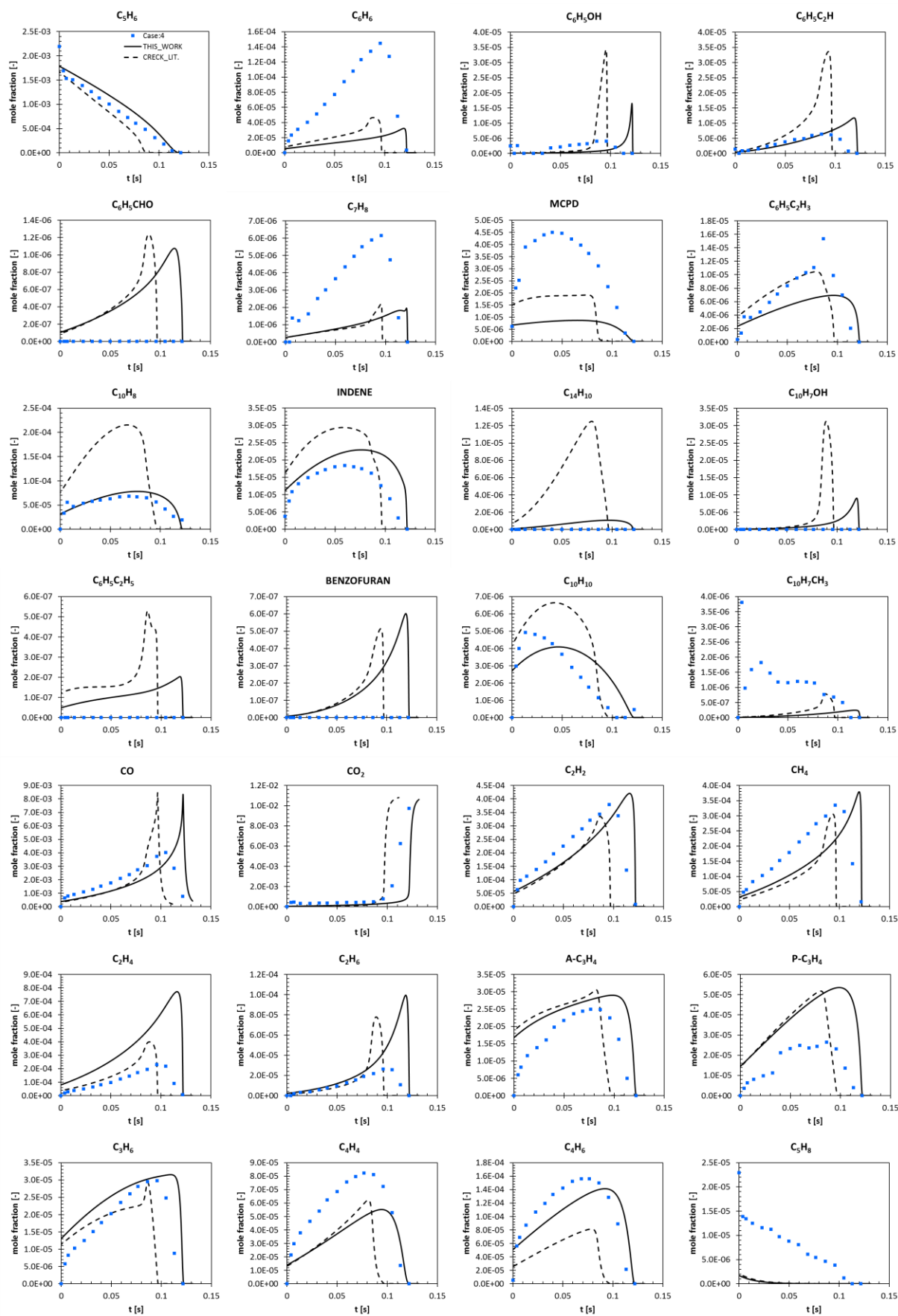
Figure S32: Species profiles in the plug flow reactor experiments of Butler et al. (T = 1150 K, P = 1 atm, phi = 0.61)[29]

d. Anisole pyrolysis and oxidation

Pyrolysis
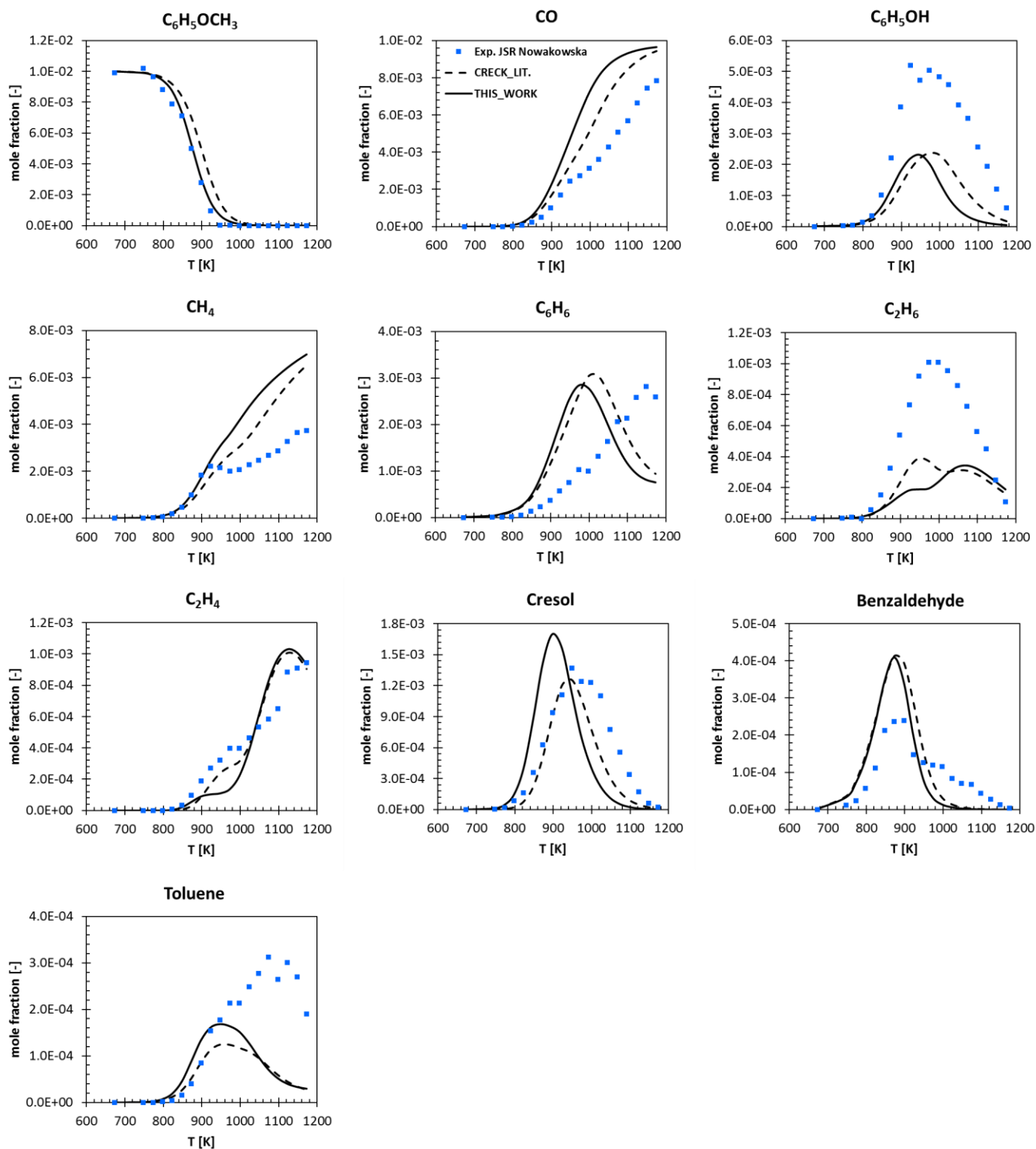
Figure S33: Species profiles of the Jet stirred reactor experiments of Nowakowska et al.[30] (P = 1 atm)
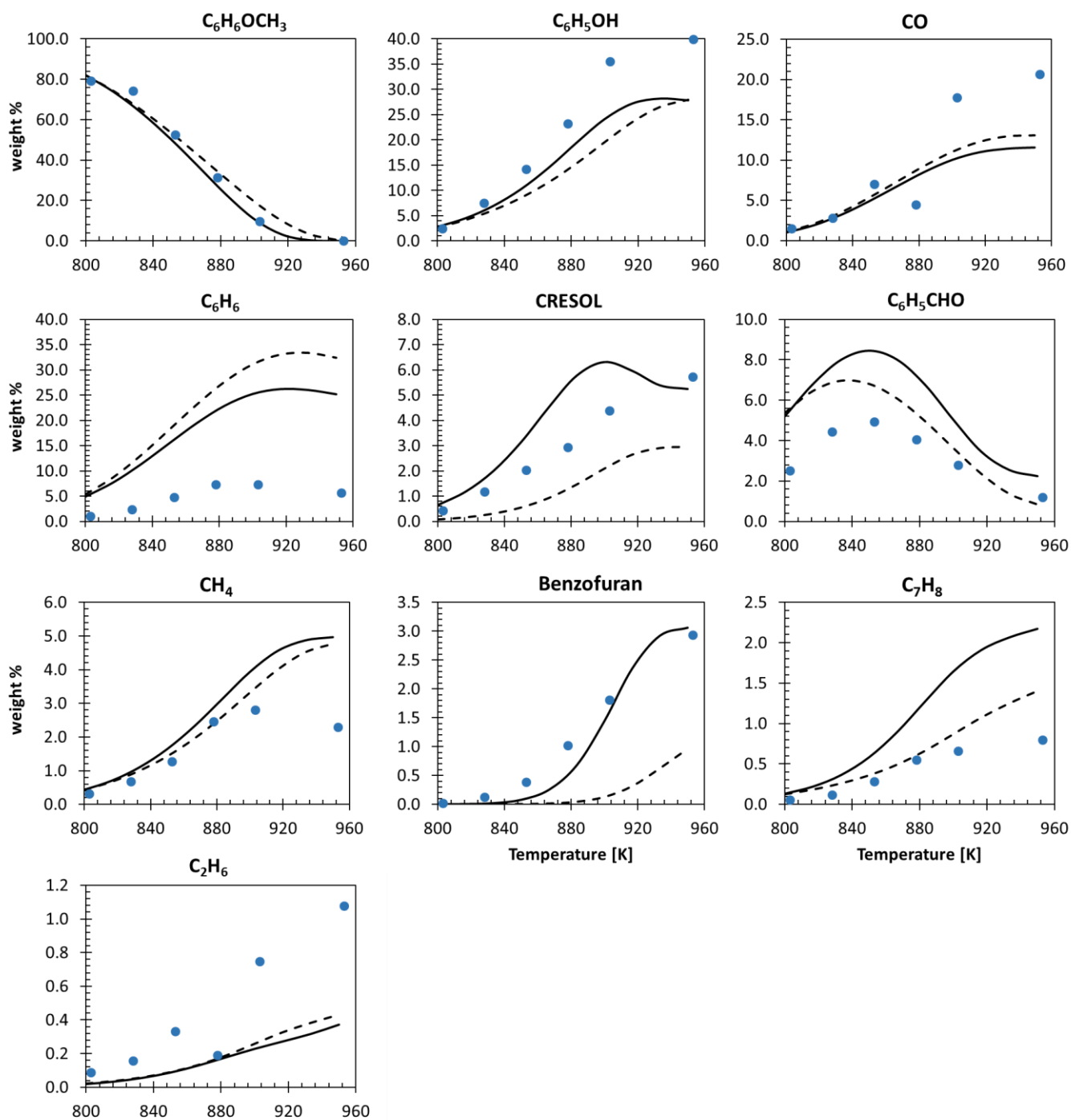
Figure S34: Species profiles in the Ghent plug flow reactor experiments (P = 1 atm)[31]
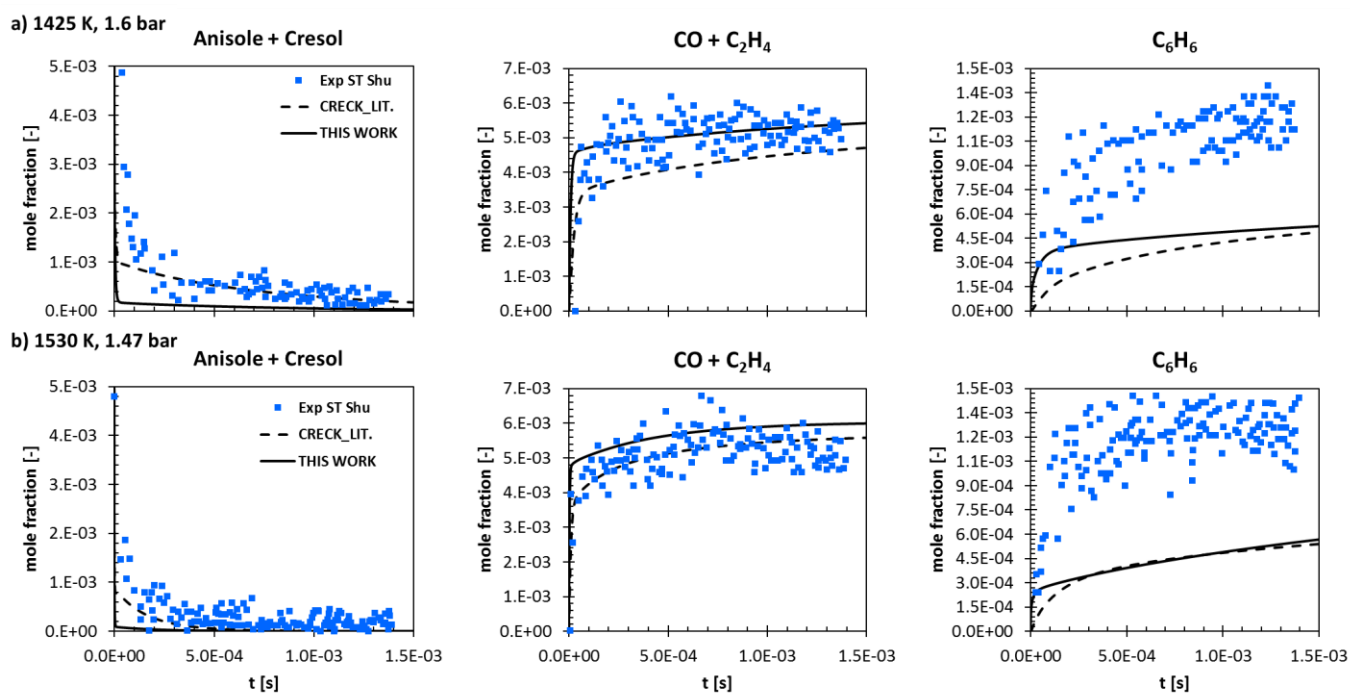
Figure S35: Species profiles in the Shock tube experiments of Shu et al., at the conditions specified in labels a) and b)[32]

Oxidation
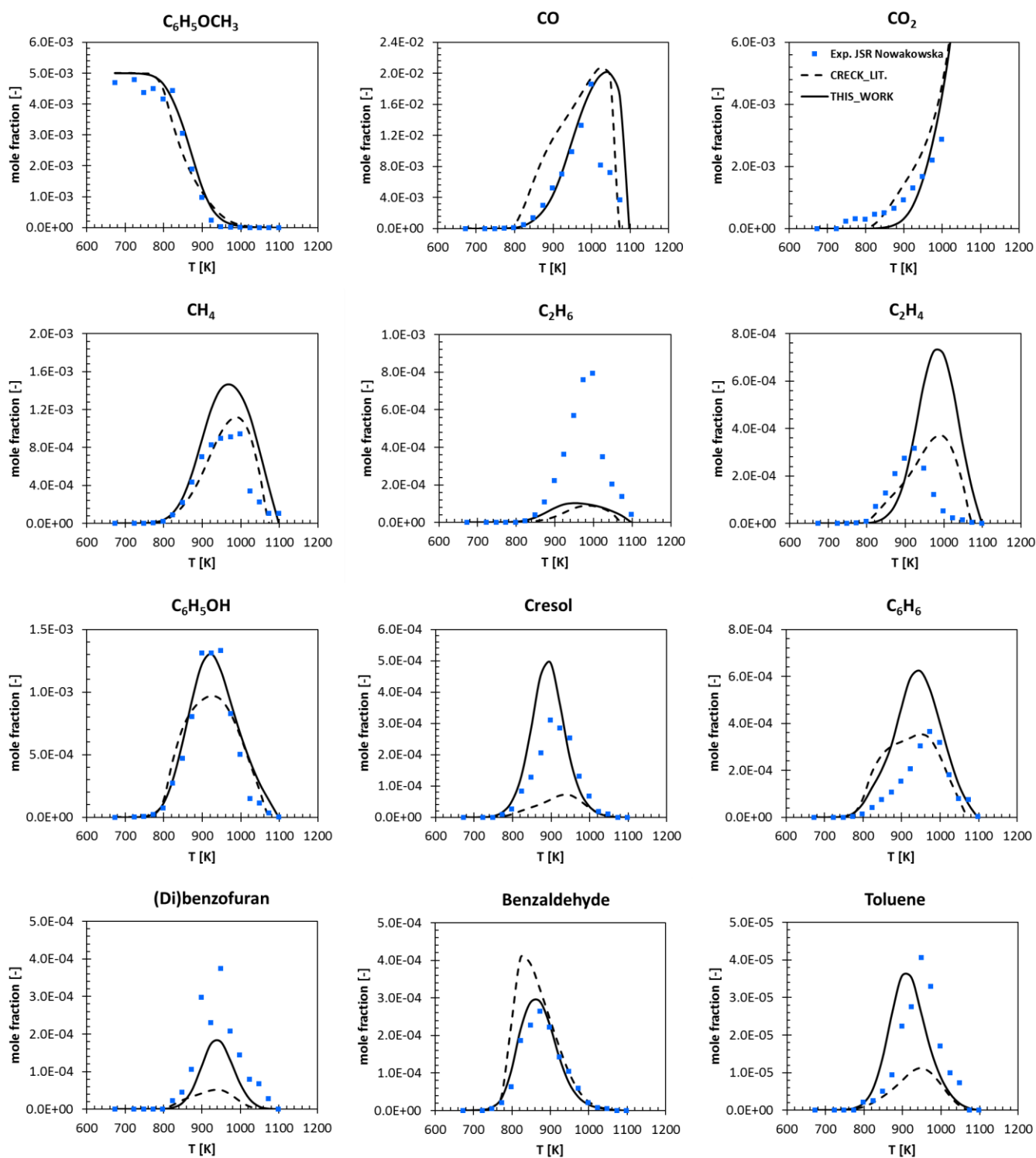
Figure S36: Species profiles of the Jet stirred reactor experiments of Nowakowska et al.[30] (phi = 1, P = 1 atm)
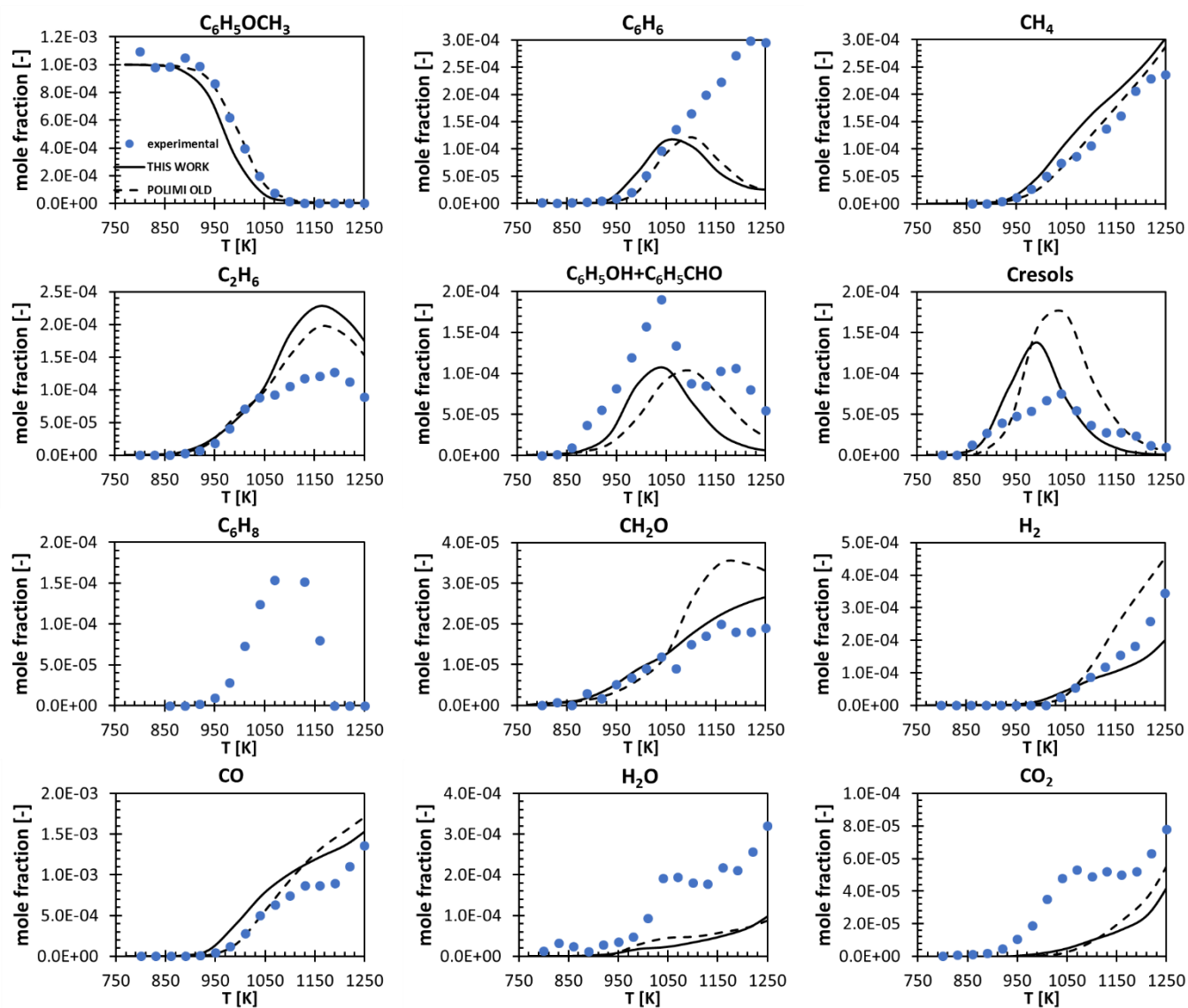
Figure S37: Species profiles of the jet stirred reactor experiments of Wagnon et al. (P = 1 atm, phi = 2)[33]
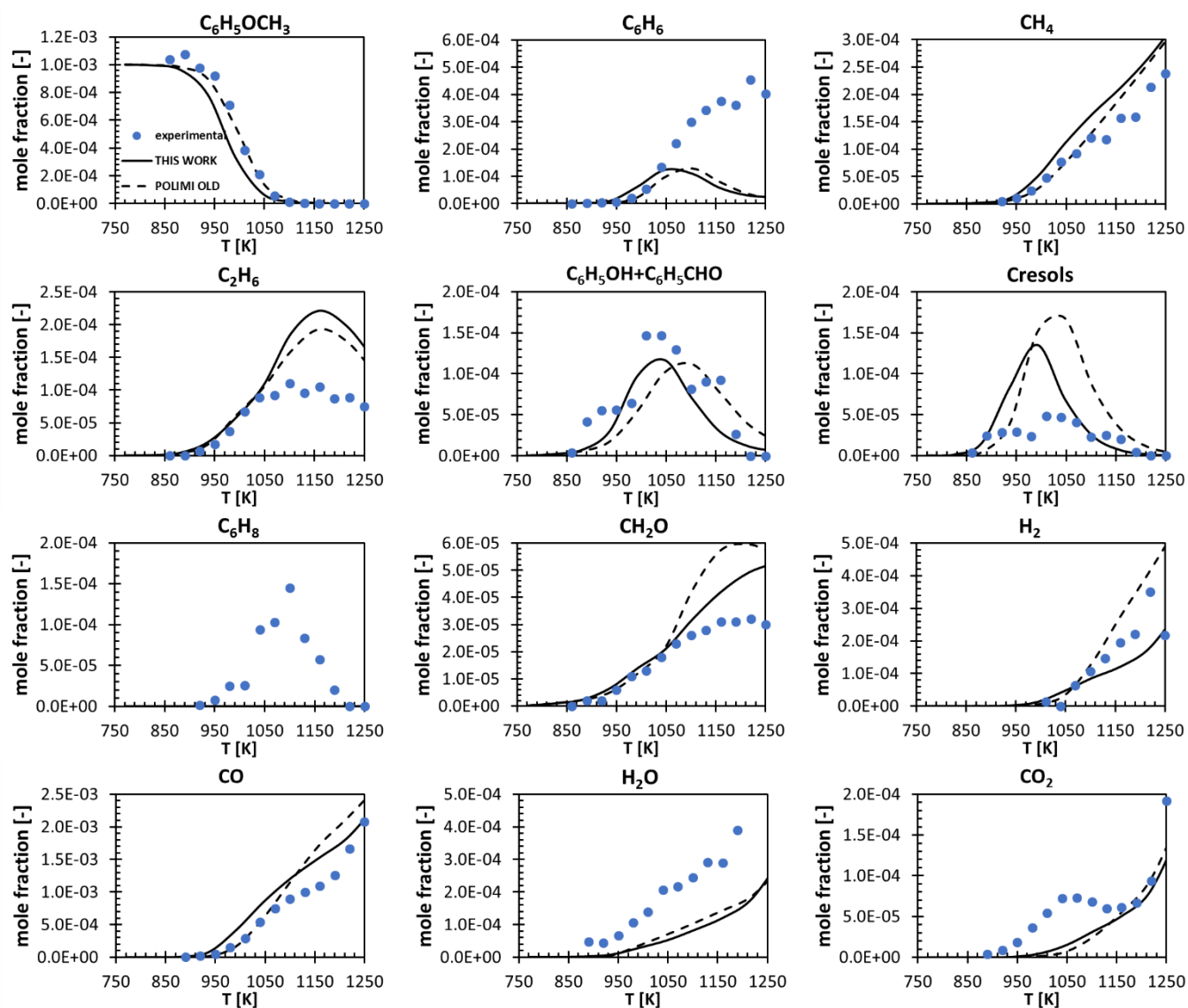
Figure S38: Species profiles of the jet stirred reactor experiments of Wagnon et al. (P = 1 atm, phi = 1)[33]
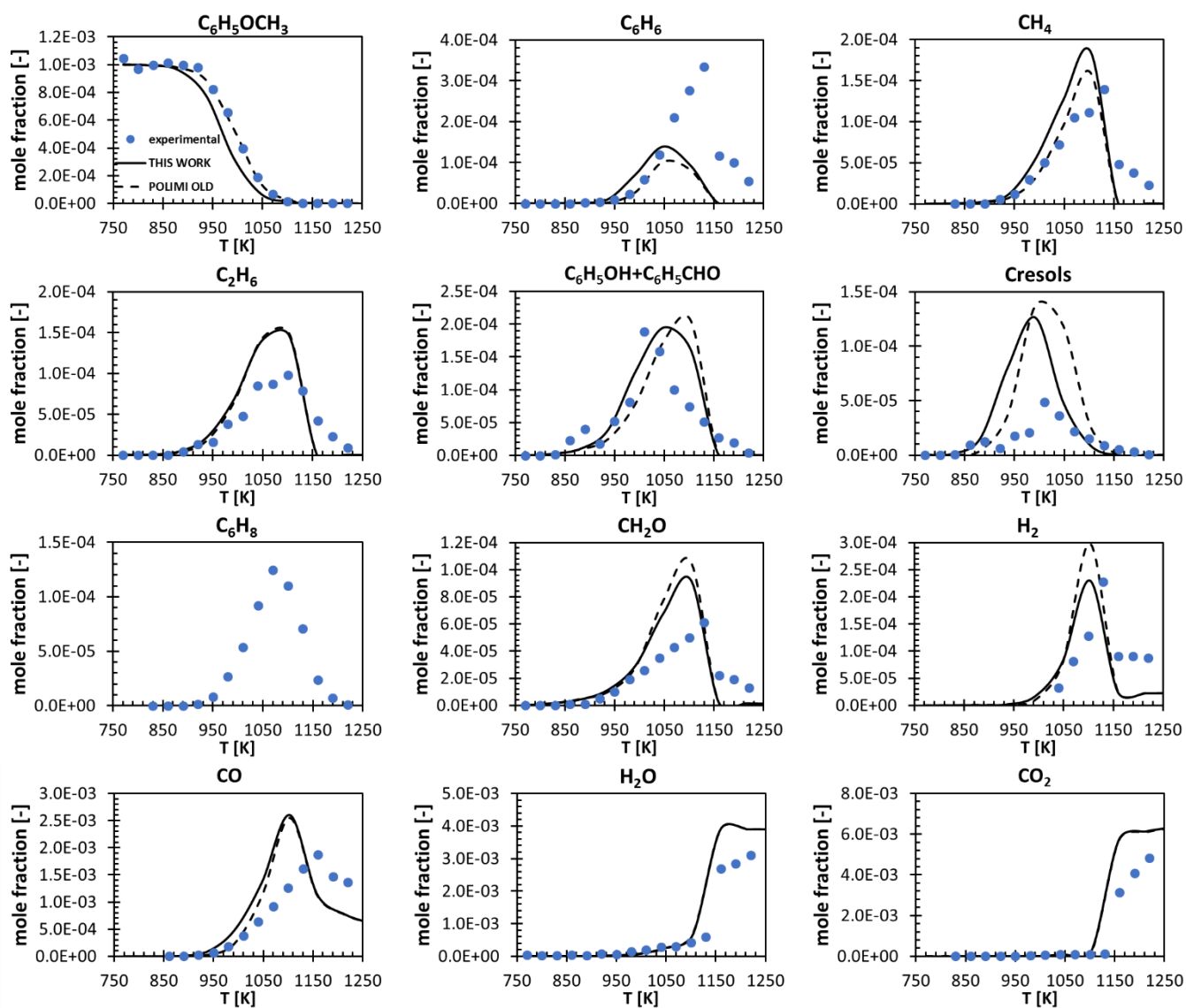
Figure S39: Species profiles of the jet stirred reactor experiments of Wagnon et al. (P = 1 atm, phi = 0.5)[33]
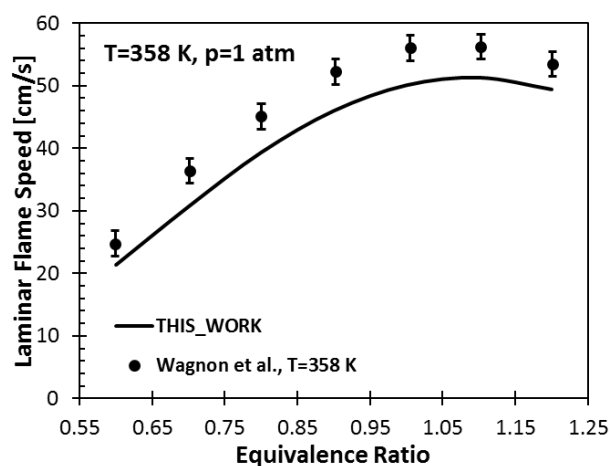
Figure S40: Laminar flame speed of anisole in the experiments of Wagnon et al.[33]
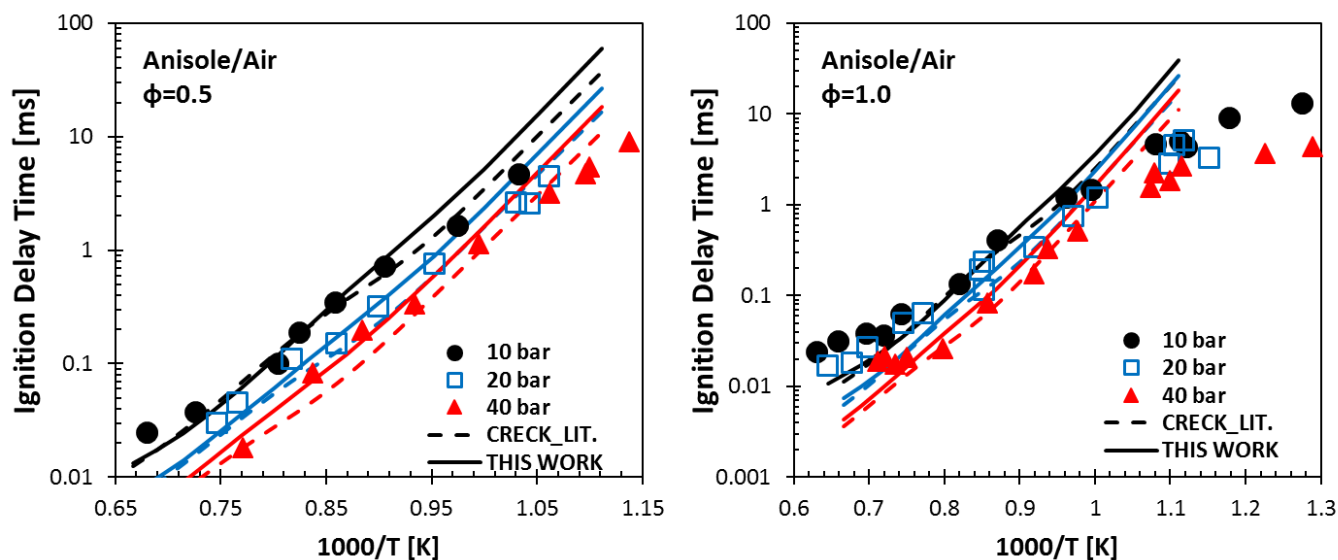
Figure S41: Ignition delay times in the ST experiments of Herzler et al.[34] (Experimental conditions specified in the plots)
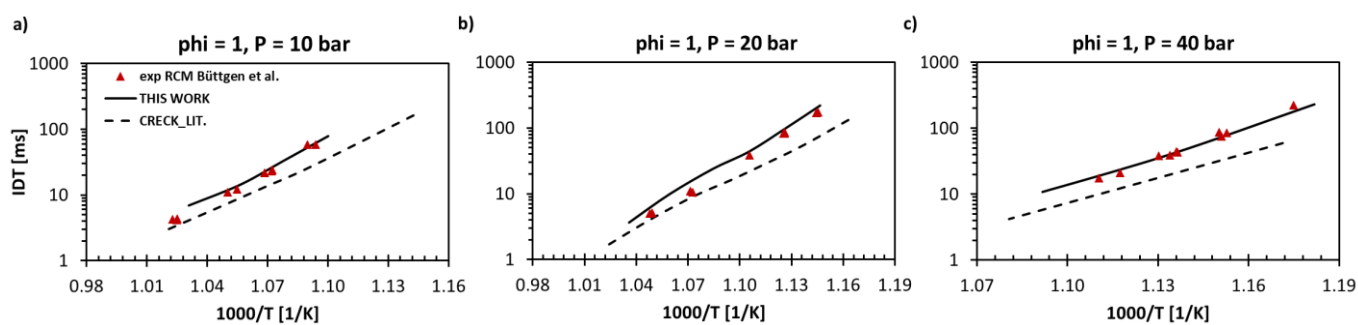
Figure S42: Ignition delay times in the RCM experiments of Büttgen et al.[35] (Experimental conditions specified in the plots)

e. Catechol, guaiacol and vanillin pyrolysis and oxidation
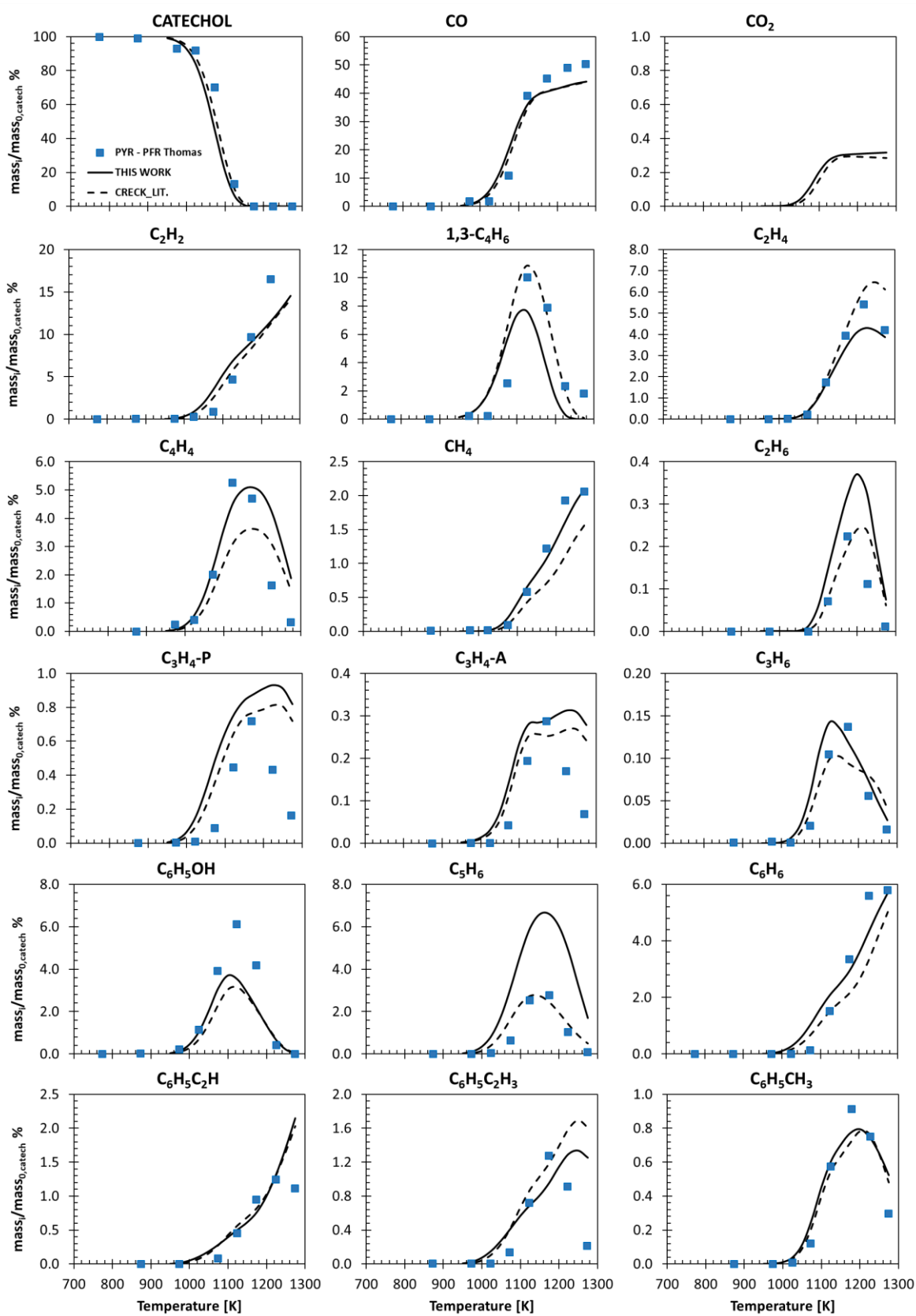
Figure S43: Species profiles of the plug flow reactor experiments of Thomas et al.,[36] in pyrolysis conditions (P atm)
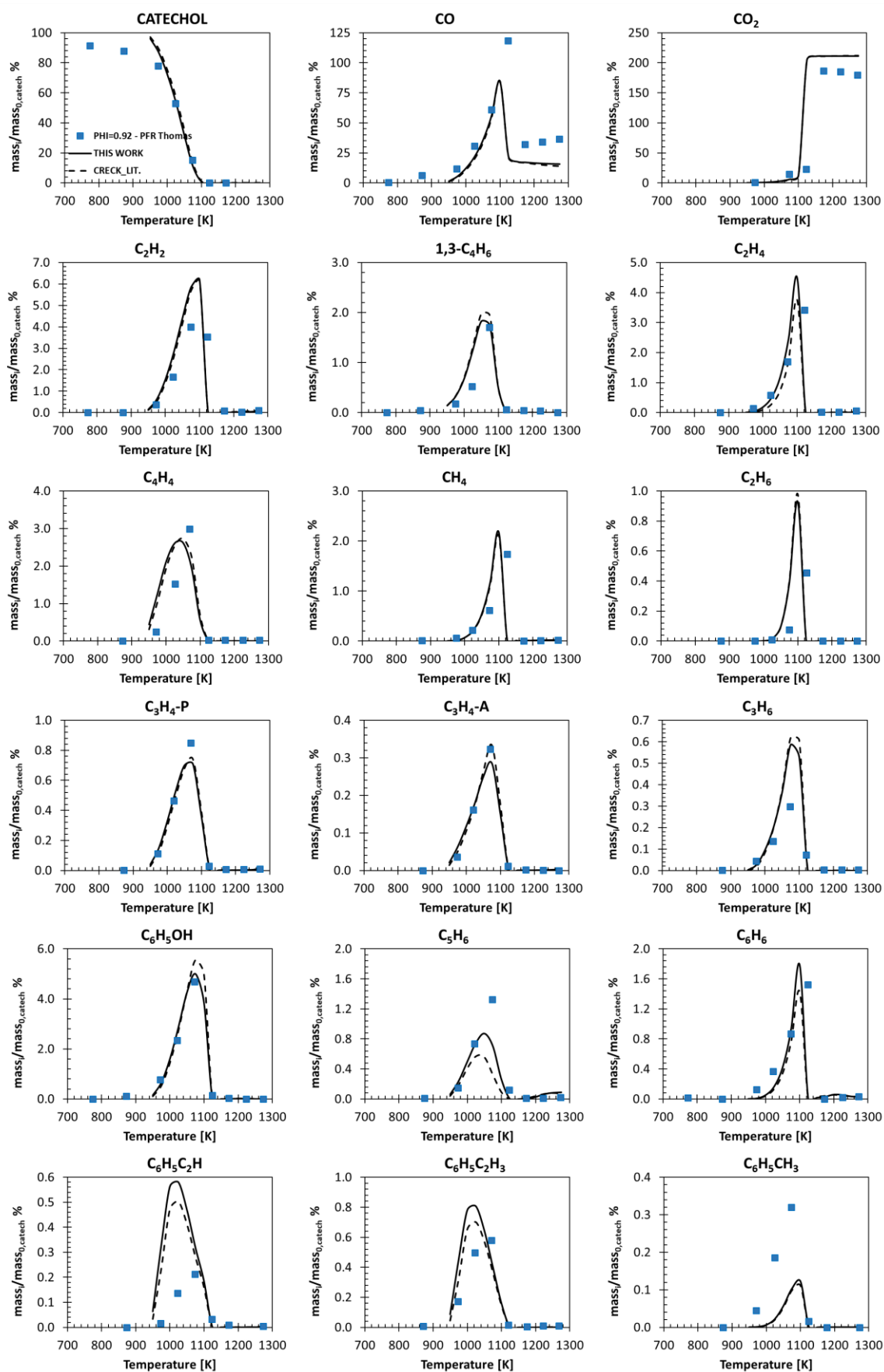
Figure S44: Species profiles of the plug flow reactor experiments of Thomas et al.,[36] (phi = 0.92)
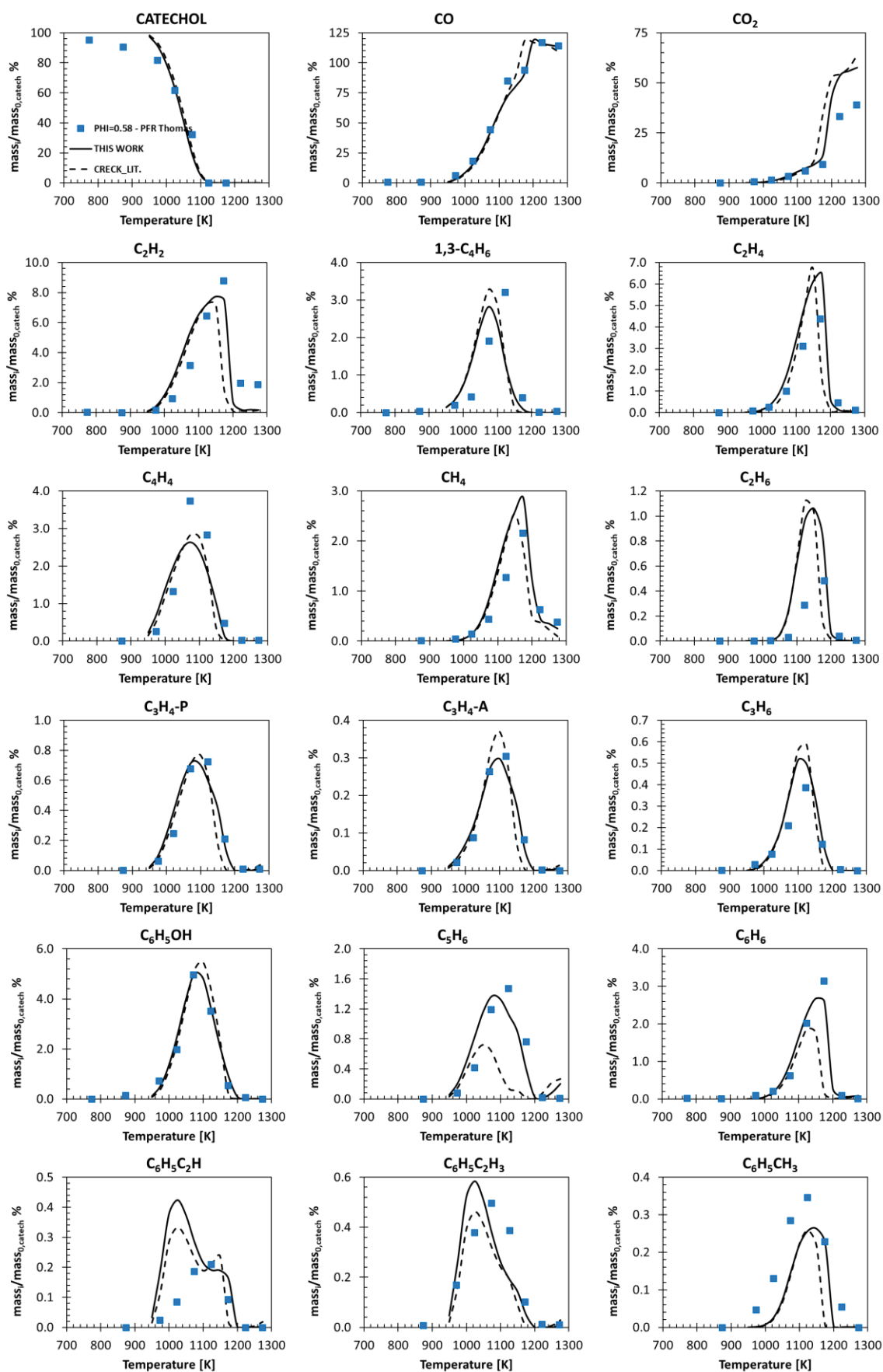
Figure S45: Species profiles of the plug flow reactor experiments of Thomas et al.,[36] (phi = 0.58)
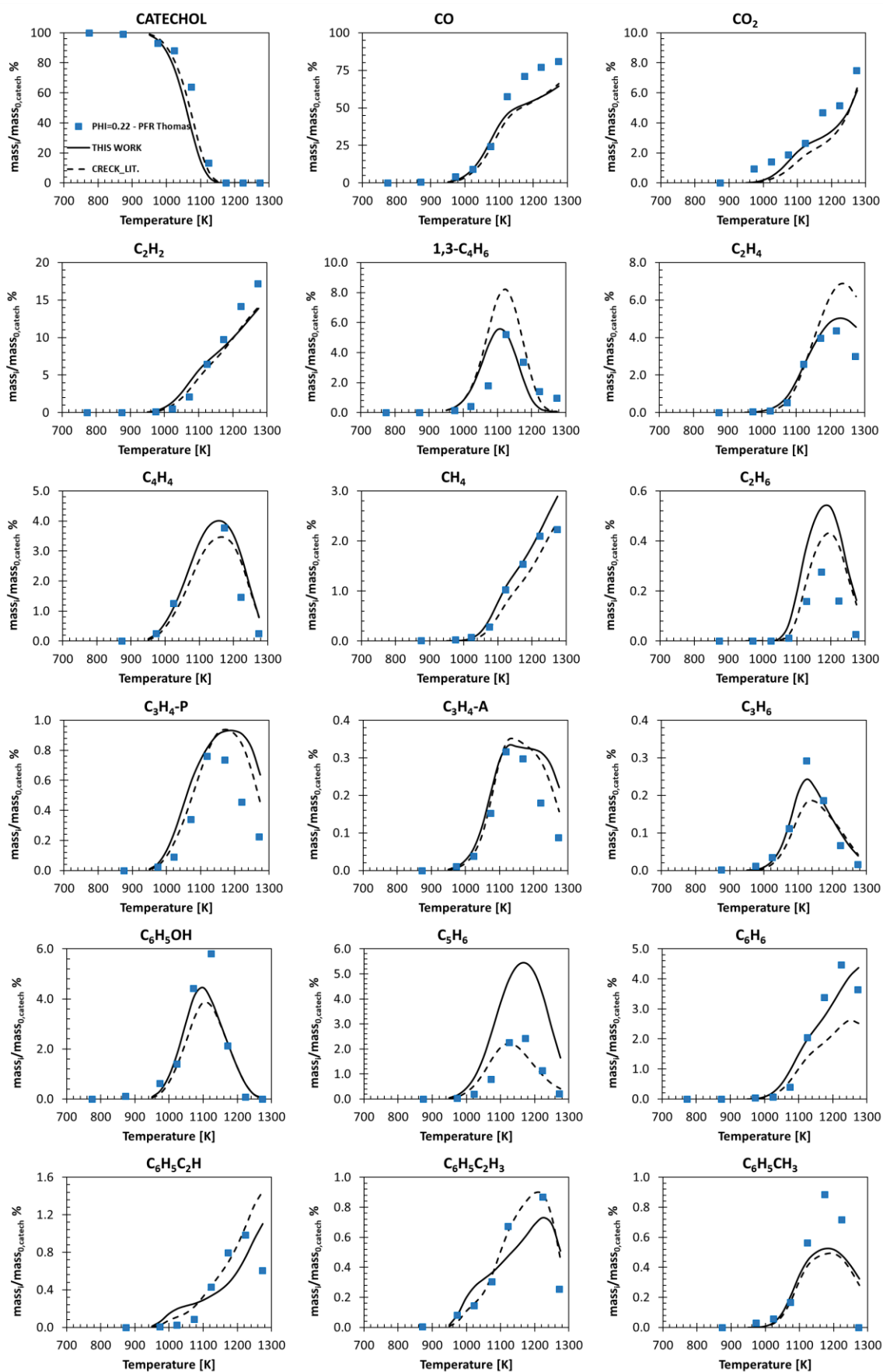
Figure S46: Species profiles of the plug flow reactor experiments of Thomas et al.,[36] (phi = 0.22)

a) Pure butadiene
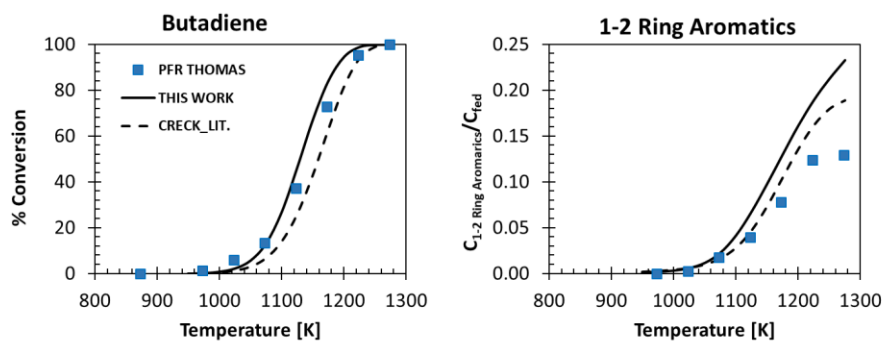
b) Pure catechol
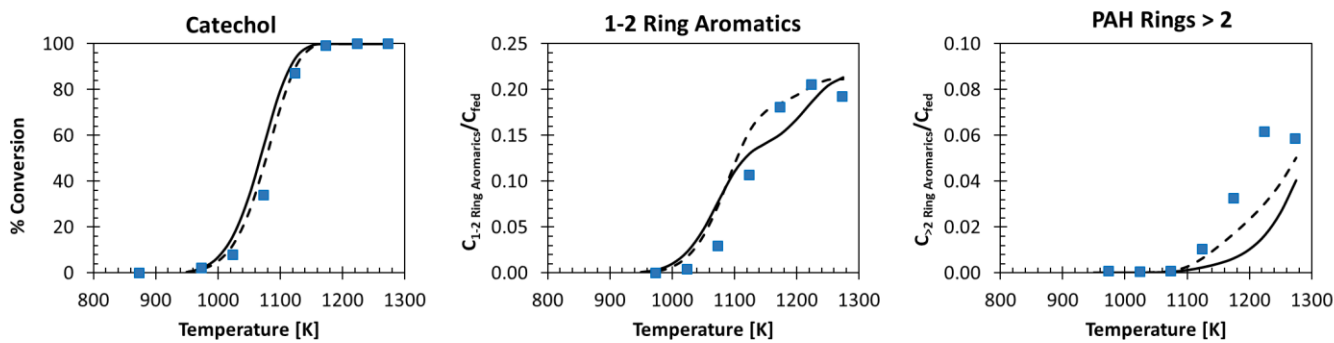
c) Mixture catechol + butadiene
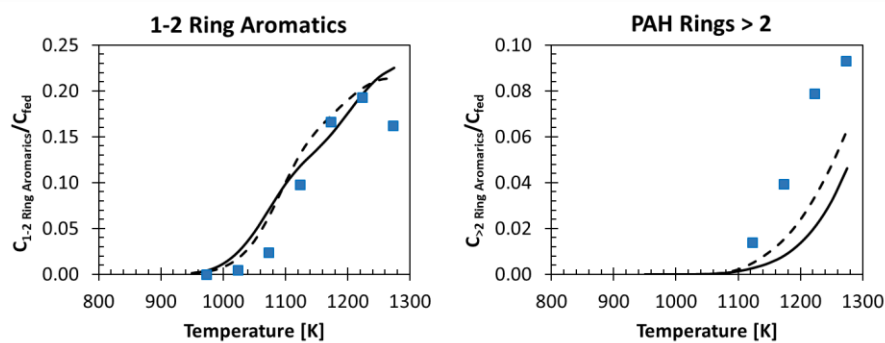
Figure S47: Species profiles of the plug flow reactor experiments of the co-pyrolysis of catechol and butadiene of Thomas et al.[37]
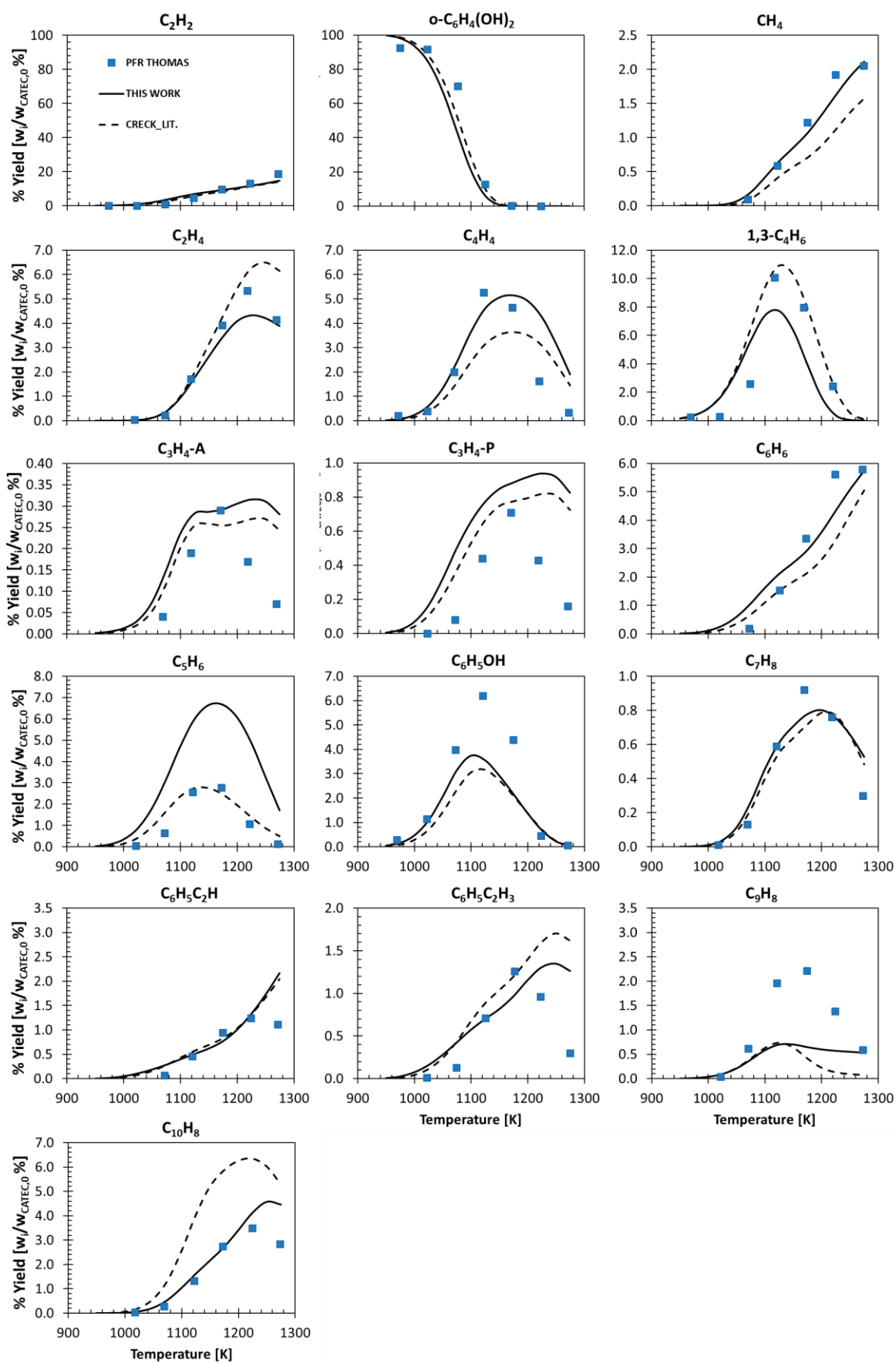
Figure S48: Species profiles of the plug flow reactor experiments of catechol pyrolysis of Poddar et al.[38]
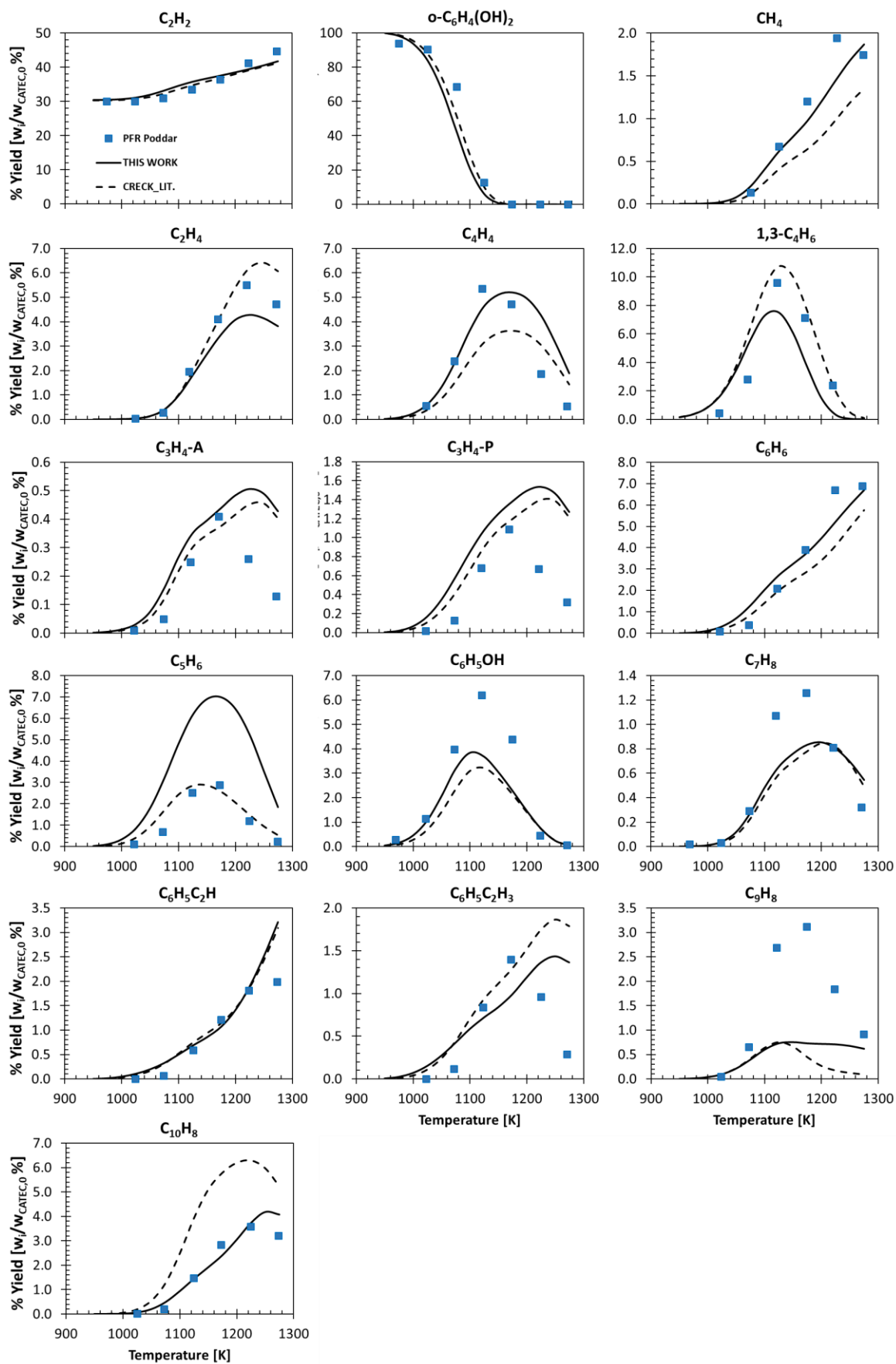
Figure S49: Species profiles of the plug flow reactor experiments of catechol and acetylene co-pyrolysis of Poddar et al.[38]
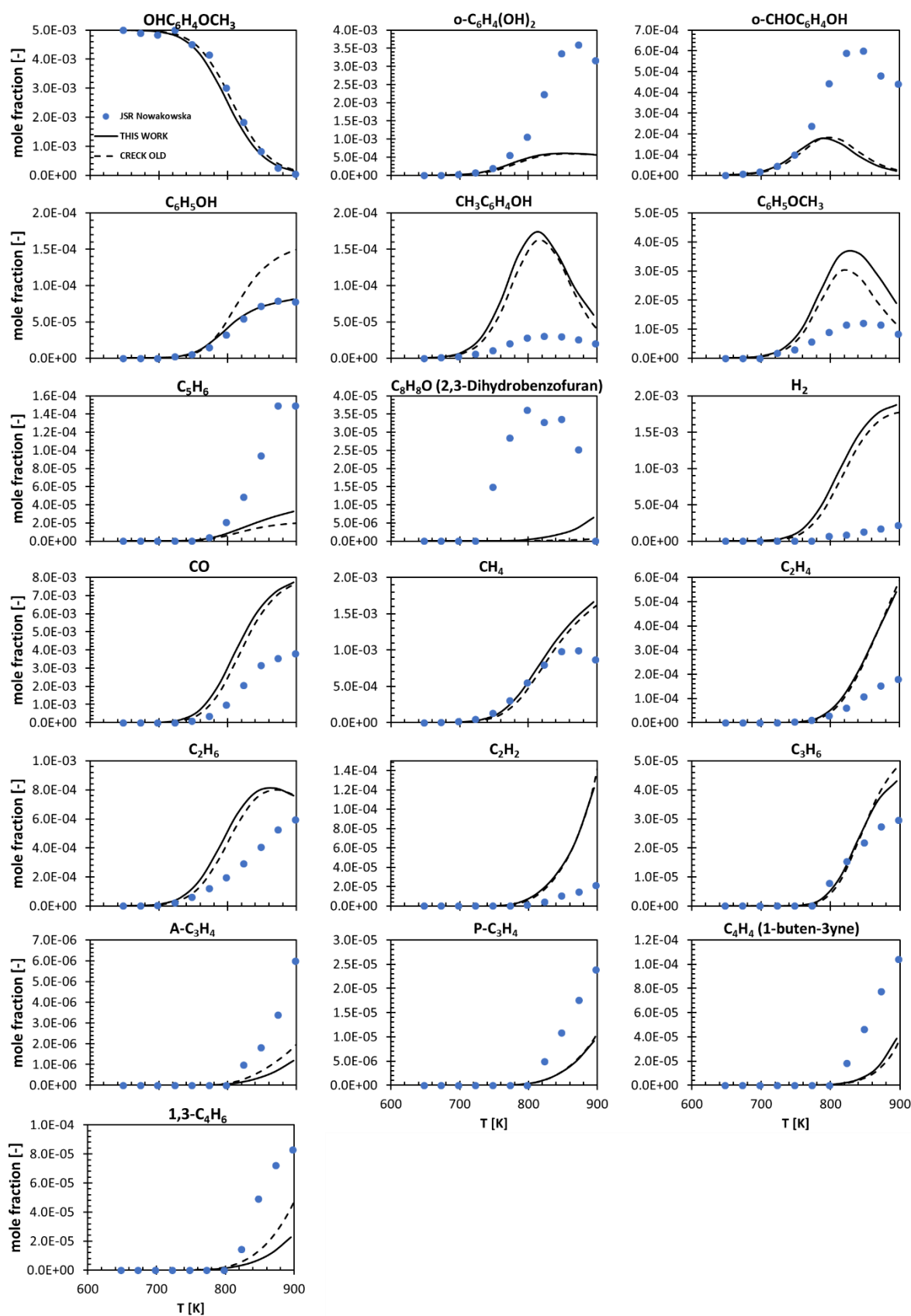
Figure S50: Species profiles of the jet stirred reactor experiments of guaiacol pyrolysis of Nowakowska et al.[39]
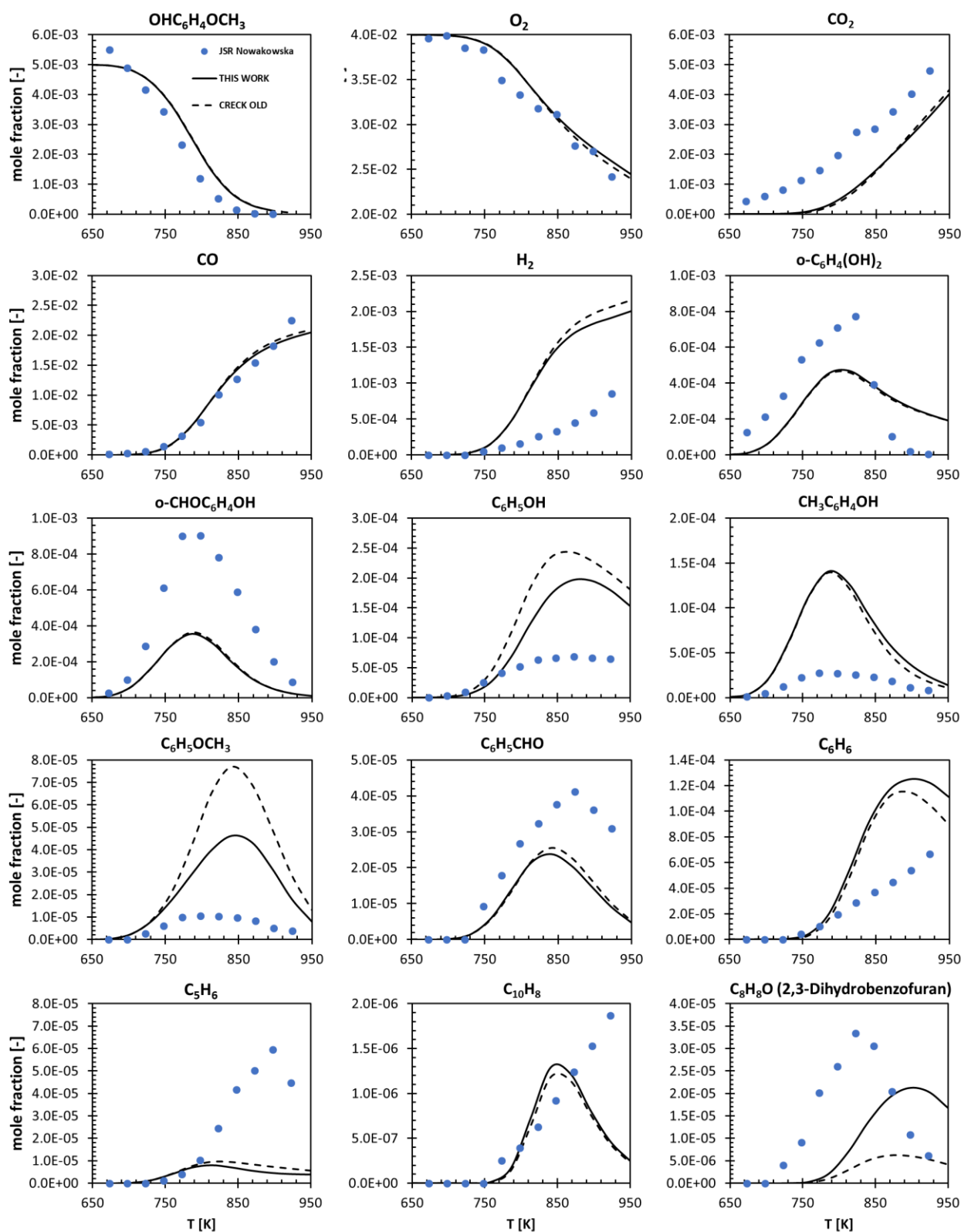
Figure S51: Species profiles of the jet stirred reactor experiments of guaiacol oxidation (phi=1) of Nowakowska et al.[39]
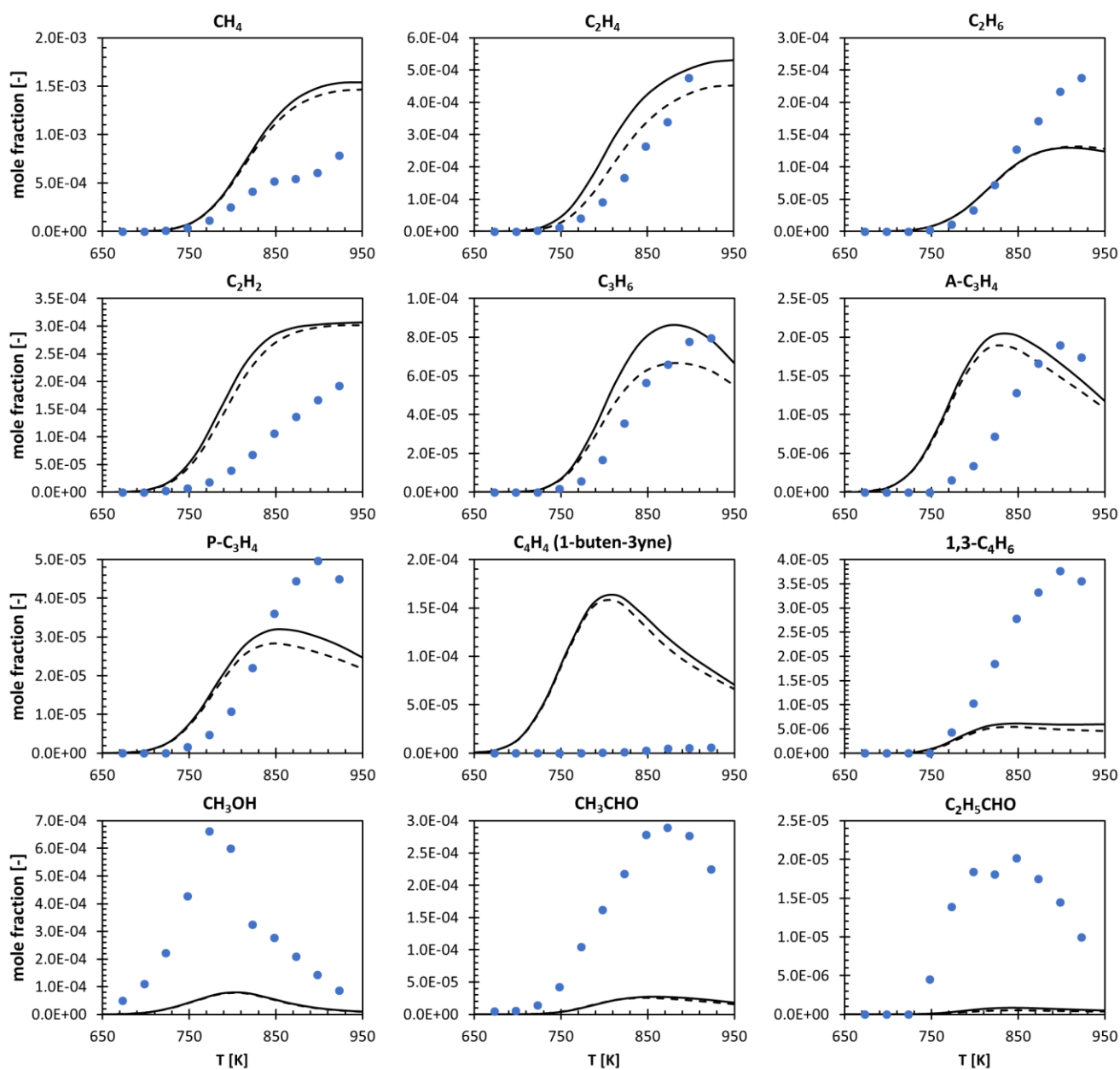
Figure S52: Species profiles of the jet stirred reactor experiments of guaiacol oxidation (phi=1) of Nowakowska et al.[39]
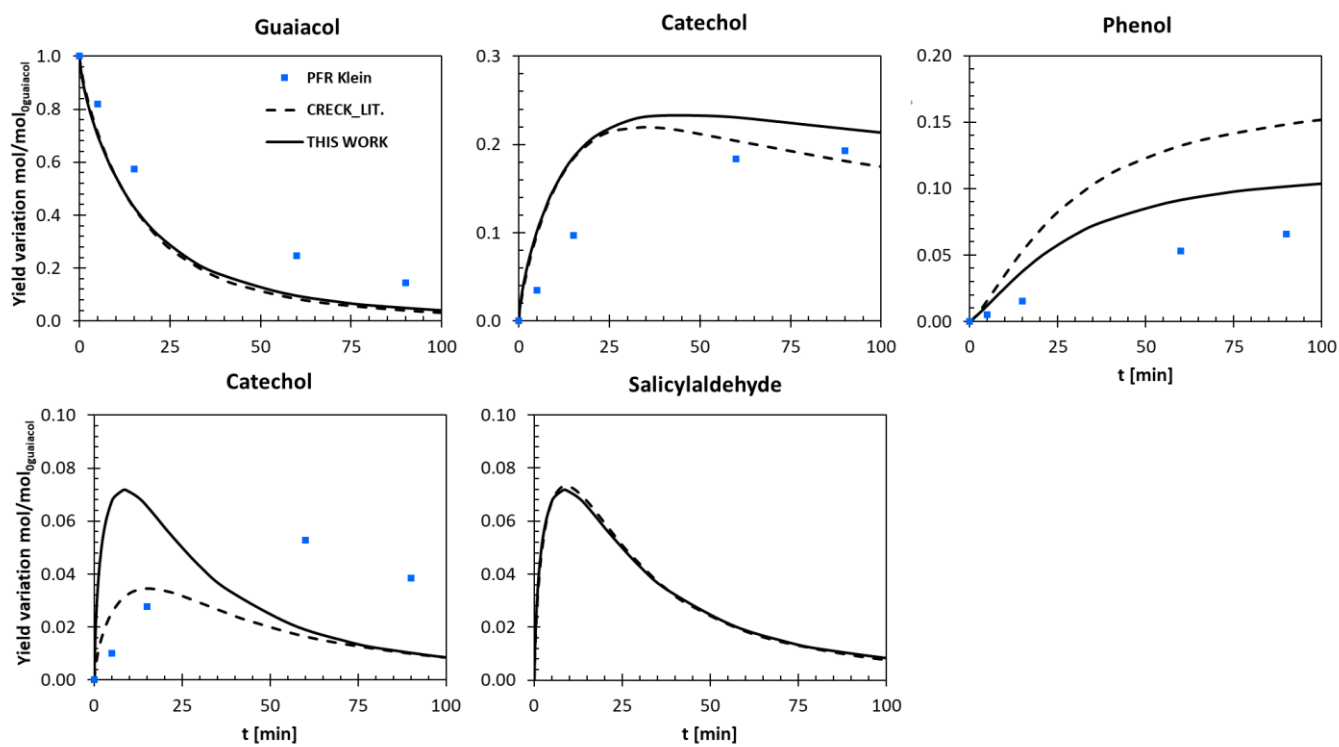
Figure S53: Species profiles of the plug flow reactor experiments of guaiacol pyrolysis of Jegers and Klein[40]

References

1   Z. F. Xu and M. C. Lin, *J. Phys. Chem. A*, 2006, **110**, 1672–1677.

2   A. M. Scheer, C. Mukarakate, D. J. Robichaud, M. R. Nimlos, H.-H. Carstensen and G. B. Ellison, *J. Chem. Phys*, 2012, **136**, 44309.

3   A. Jalan, I. M. Alecu, R. Meana-Pañeda, J. Aguilera-Iparraguirre, K. R. Yang, S. S. Merchant, D. G. Truhlar and W. H. Green, *J. Am. Chem. Soc.*, 2013, **135**, 11100–11114.

4   T. J. Lee and P. R. Taylor, *Int. J. Quantum Chem. Quantum Chem. Symp. 23*, 1989, 199–207.

5   N. E. Schultz, Y. Zhao and D. G. Truhlar, *J. Phys. Chem. A*, 2005, **109**, 11127–11143.

6   N. E. Schultz, B. F. Gherman, C. J. Cramer and D. G. Truhlar, *J. Phys. Chem. B*, 2006, **110**, 24030–24036.

7   A. Karton, E. Rabinovich, J. M. L. Martin and B. Ruscic, *J. Chem. Phys.*, 2006, **125**, 144108.

8   O. Tishchenko, J. Zheng and D. G. Truhlar, *J. Chem. Theory Comput.*, 2008, **4**, 1208–1219.

9   A. B. Lovell, K. Brezinsky and I. Glassman, *Int. J. Chem. Kinet.*, 1989, **21**, 547–560.

10   M. U. Alzueta, P. Glarborg and K. Dam-Johansen, *Int. J. Chem. Kinet.*, 2000, **32**, 498–522.

11   R. D. Kern and C. H. Wu, *Twent. Symp. Combust. Combust. Inst.*, 1984, **2**, 789–797.

12   A. Laskin and A. Lifshitz, *Twenty-Sixth Symp. Combust. Combust. Inst.*, 2000, 669–675.

13   R. Sivaramakrishnan, K. Brezinsky, H. Vasudevan and R. S. Tranter, *Combust. Sci. Technol.*, 2006, **178**, 285–305.

14   Y. Chai and L. D. Pfefferle, *Fuel*, 1998, **77**, 313–320.

15   I. Da Costa, R. Fournet, F. Billaud and F. Battin-Leclerc, *Int. J. Chem. Kinet.*, 2003, **35**, 503–524.

16   In *Proceedings of the Joint Meeting of the French and German Sections of the Combustion Institute, Mulhouse*, pp. 11–13.

17   A. Ristori, P. Dagaut, A. El Bakali, G. Pengloan and M. Cathonnet, *Combust. Sci. Technol.*, 2001, **167**, 223–256.

18   A. B. Lovell, K. Brezinsky and I. Glassman, *Symp. Combust.*, 1989, **22**, 1063–1074.

19   C. Venkat, K. Brezinsky and I. Glassman, *Symp. Combust.*, 1982, **19**, 143–152.

20   D. A. Bittker, *Oxidation Mechanisms Toluene and Benzene Oxidation Mechanisms of Toluene and Benzene*, .

21   C. Ji, E. Dames, H. Wang and F. N. Egolfopoulos, *Combust. Flame*, 2012, **159**, 1070–1081.

22   R. J. Johnston and J. T. Farrell, *Proc. Combust. Inst.*, 2005, **30**, 217–224.

23   S. G. Davis and C. K. Law, *Combust. Sci. Technol.*, 1998, **140**, 427–449.

24   M. R. Djokic, K. M. Van Geem, C. Cavallotti, A. Frassoldati, E. Ranzi and G. B. Marin, *Combust. Flame*, 2014, **161**, 2739–2751.

25   D. H. Kim, J. A. Mulholland, D. Wang and A. Violi, *J. Phys. Chem. A*, 2010, **114**, 12411–12416.

26   A. J. Vervust, M. R. Djokic, S. S. Merchant, H.-H. Carstensen, A. E. Long, G. B. Marin, W. H. Green and K. Van Geem, *Energy & Fuels*, 2018, **32**, 3920–3934.

27   C. Ji, R. Zhao, B. Li and F. N. Egolfopoulos, *Proc. Combust. Inst.*, 2013, **34**, 787–794.

28   J. Orme, H. Curran and J. Simmie, *Proc. Eur. Combust. Meet.*

29   R. G. Butler and I. Glassman, *Proc. Combust. Inst.*, 2009, **32 I**, 395–402.

30   M. Nowakowska, O. Herbinet, A. Dufour and P.-A. Glaude, *Combust. Flame*, 2014, **161**, 1474–1488.

31   E. Ranzi, M. Costa, M. Pelucchi, T. Faravelli, A. Frassoldati, G. Sribala, G. B. Marin and K. M. Van Geem, in *Chemical Engineering Transactions*, 2018, vol. 65.

32   B. Shu, J. Herzler, S. Peukert, M. Fikri and C. Schulz, *Int. J. Chem. Kinet.*, 2017, **49**, 656–667.

33   S. W. Wagnon, S. Thion, E. J. K. Nilsson, M. Mehl, Z. Serinyel, K. Zhang, P. Dagaut, A. A. Konnov, G. Dayma and W. J. Pitz, *Combust. Flame*, 2018, **189**, 325–336.

34   J. Herzler, M. Fikri and C. Schulz, *Ignition Delay Time Study of Aromatic LIF Tracers in a Wide Temperature and Pressure Range*, .

35   R. D. Büttgen, L. Pratali Maffei, M. Pelucchi, T. Faravelli, A. Frassoldati and K. A. Heufer, in *9th European Combustion Meeting*, 2019, pp. 1–7.

36   S. Thomas, E. B. Ledesma and M. J. Wornat, *Fuel*, 2007, **86**, 2581–2595.

37   S. Thomas and M. J. Wornat, *Proc. Combust. Inst.*, 2009, **32**, 615–622.

38   N. B. Poddar, S. Thomas and M. J. Wornat, *Proc. Combust. Inst.*, 2011, **33**, 541–548.

39   M. Nowakowska, O. Herbinet, A. Dufour and P. A. Glaude, *J Phys Chem A*, 2018, **122**, 7894–7909.

40   H. E. Jegers and M. T. Klein, *Ind. Eng. Chem. Process Des. Dev*, 1985, **24**, 173–183.